



저작자표시-비영리-변경금지 2.0 대한민국

이용자는 아래의 조건을 따르는 경우에 한하여 자유롭게

- 이 저작물을 복제, 배포, 전송, 전시, 공연 및 방송할 수 있습니다.

다음과 같은 조건을 따라야 합니다:



저작자표시. 귀하는 원저작자를 표시하여야 합니다.



비영리. 귀하는 이 저작물을 영리 목적으로 이용할 수 없습니다.



변경금지. 귀하는 이 저작물을 개작, 변형 또는 가공할 수 없습니다.

- 귀하는, 이 저작물의 재이용이나 배포의 경우, 이 저작물에 적용된 이용허락조건을 명확하게 나타내어야 합니다.
- 저작권자로부터 별도의 허가를 받으면 이러한 조건들은 적용되지 않습니다.

저작권법에 따른 이용자의 권리는 위의 내용에 의하여 영향을 받지 않습니다.

이것은 [이용허락규약\(Legal Code\)](#)을 이해하기 쉽게 요약한 것입니다.

[Disclaimer](#)

이학박사 학위논문

Study of the rupture process of nanometer
water bridge by using time-resolved noncontact
AFM

시간분해능 비접촉 원자힘 현미경을 이용한 나노크기 물기등의
파열과정에 관한 연구

2015년 2월

서울대학교 대학원

물리·천문학부

박 완

Study of the rupture process of nanometer water bridge
by using time-resolved noncontact AFM

시간분해능 비접촉 원자힘 현미경을 이용한 나노크기 물기둥의
파열과정에 관한 연구

指導教授 諸元鎬

이 論文을 理學博士學位論文으로 提出함

2014年 11月

서울대학교 大學院

物理·天文學部

朴 完

朴完의 理學博士 學位論文을 認准함

2014年 12月

委 員 長	박 건 식	印
副 委 員 長	제 원 호	印
委 員	홍 성 철	印
委 員	이 진 호	印
委 員	곽 호 영	印

**Study of the rupture process of nanometer
water bridge by using time-resolved noncontact
AFM**

by

Wan Bak, M.S.

Dissertation

Presented to the Faculty of the Graduate School of

Seoul National University

in Partial Fulfillment

of the Requirements

for the Degree of

Doctor of Philosophy

Seoul National University

February 2015

Abstract

Study of the rupture process of nanometer water bridge by using time-resolved noncontact AFM

Wan Bak

Department of Physics and Astronomy
The Graduate School
Seoul National University

The nanometric water bridge is formed by capillary condensation between two close bodies in ambient condition, and is a commonplace phenomenon in nature. The water bridge plays an important role in the dynamic processes such as friction, adhesion and solvation, and is widely used in nanotechnology including dip-pen lithography, atomic force microscopy (AFM) and micro-electro-mechanical systems. Recently, it has been well known that the water bridge is essential in understanding the biological mechanisms of the ion-channel and protein folding. Therefore, it is important to have better and broader understanding of the mechanics, dynamics as well as kinetics of the capillary-condensed water bridge in ambient condition, from its formation to rupture.

There have been extensive studies on the formation of the capillary water nanobridges over the last several decades. In most previous theoretical studies, the Kelvin-Laplace equation has been used to determine the size and shape of the water bridge, which forms at the nanoscopic contacts of solid surfaces.

In particular, if the water bridge is formed in thermodynamic equilibrium, the radius of curvature of the bridge is equal to the Kelvin radius, and thus the bridge should break up or rupture at the distance equal to twice the Kelvin radius.

However, the applicability of this approach to the capillary bridge at the nanoscale is still in debate. Based on the experimental observation and theoretical model of the water bridge, Riedo et al. have found that the volume of the stretched water bridge is proportional to the rupture distance. Because the curvature radius of the water bridge changed during the tip retraction, the state of the water bridge is not in thermodynamic equilibrium. From the results, they found that the stretched water bridge breaks up a distance that is much larger than twice of the Kelvin radius.

In thermodynamic nonequilibrium, the rupture process of the water bridge is associated with the chemical potential gradients that may result in material transfer and trigger the irreversible bridge rupture. Thus, the Kelvin equation is not applicable in thermodynamic nonequilibrium. Men et al. applied the density functional theory, which is based on the energy barrier, in order to study the rupture process of the water bridge. Their work demonstrated the origin of the hysteresis behavior in the formation and rupture of the water bridge, and the rupture started by overcoming the energy barrier, which is so called the thermal activation process.

Despite the established theoretical results, however, experimental works on the kinetics of the nanoscale rupture process in terms of thermal activation

still lack, unlike the well studied capillary formation.

In this Letter, we directly measure the activation time needed for the water bridge to be ruptured by using the quartz-tuning-fork (QTF) based AFM in ambient condition. We find that the activation time obtained at the various rupture distance exhibits random distribution and shows the characteristic exponential decay, which indicates that the rupture process follows the Poisson statistics, which is typical of the thermal activation processes. We also have measured the dependence of the rupture rate on the tip-sample distance as well as the temperature, from which we can estimate the values of the activation energy.

Keywords : time-resolved noncontact AFM, QTF-AFM, water nanobridge, rupture, thermally activation process

Student number : 2009-30096

Contents

Abstract	i
List of Figures	vii
Chapter 1 Introduction	1
1.1 Rupture kinetics of capillary-condensed water nanobridge	1
1.2 Time-resolved dynamic force microscopy by QTF based AFM . .	3
1.3 Outline of this thesis	5
Chapter 2 Quartz Tuning-Fork for Force Measurement	9
2.1 Introduction	9
2.2 Electrical Driven Quartz Tuning-Fork	10
2.3 Mechanical Oscillation Amplitude of QTF	14
2.4 Electrical modulation QTF as a Force Sensor	15
2.5 Conclusion	17
Chapter 3 Mechanical study of water nanobridge using QTF- AFM	20

3.1	Introduction	20
3.2	Quartz Tuning-Fork based Atomic Force Microscopy	21
3.3	Measurement of Mechanical Properties of water nanobridge	25
3.4	Conclusion	29
Chapter 4 Rupture Process of water nanobridge		31
4.1	Introduction	31
4.2	Activation Process associated with Rupture of water nanobridge	32
4.2.1	Time-Resolved Dynamic Force Microscopy	32
4.2.2	Rupture rate of water nanobridge	34
4.3	Thermal Enhancement of Rupture Rate	44
4.4	Conclusion	56
Chapter 5 Chapter 5		59
5.1	Summary and Perspective	59
Appendix A		62
A.1	Phase behavior of rupture process for water nanobridge	62
Appendix B		64
B.1	Actual and Apparent Probability	64
Appendix C		67
C.1	Spectral fluctuations on excitonic transitions of InGaAs SQDs	67
C.1.1	Introduction	67

C.1.2	Optical Fiber Probes for Low-Temperature Near-field Spectroscopy	69
C.1.3	Spectral Random Fluctuation of InGaAs SQDs	71
	초 록	82

List of Figures

2.1	(a) Schematic of RLC circuit model for electrical modulation QTF. (b) Geometrical interpretation of electrical modulation QTF is depicted. The circle (dot-and-dash line) is shifted along the y-axis as much as A_C	12
2.2	Comparison of apparent signal (open squares) and actual signal (open circles) in electrical modulation QTF, (a) amplitude. (b) of phase difference.	13
3.1	The fabricated probe tip for QTF-AFM (a) Schematic of fabrication of the probe tip for the QTF-AFM. The silicon cantilever tip attached by epoxy at one prong of QTF. (b) Optical microscope image of the glued & cut probe tip for QTF-AFM.	22
3.2	Schematic diagram of the shear-mode QTF-AFM.	24

3.3	Full approach-retraction curves by the QTF-AFM (a), (b) Approach (closed squares) / retraction (open squares) curves of the measured amplitude and phase difference as a function of the tip-sample distance H . The relative humidity and temperature are maintained at 37 % and 19.7 °C. From change of the amplitude and phase difference of the probe tip, we can define to the formation, rupture distance and contact point of water nanobridge, as denoted by H_f , H_r and $H = 0$. The four regions (marked by A, B, C and D) with respect to H show the different states associated with the water nanobridge.	26
3.4	Mechanical properties of water nanobridge by QTF-AFM. (a) Interaction stiffness k_{int} , (b) damping coefficient b_{int} and (c) energy dissipation E_{diss} . Mechanical properties can be obtained from the amplitude and phase difference results in Fig. 3.3. . . .	27
4.1	Time-resolved dynamic force microscopy (TRDFM) system. (a) The experimental system in the humidity-controlled air-tight chamber. (b)The part is focused the brass stage of the TRDFM, which is consist of the QTF probe tip and mica sample and PZT. The one-bode brass stage reduced the thermal drift speed. . . .	33

4.2	The time-resolved AFM amplitude signals near the moment of rupture of the water nanobridge. The relative humidity and temperature are maintained at 35% and 23.2 °C. (a) The oscillation amplitude of the probe tip (open circles), its time-averaged phase (red triangles) and the stepwise change of the tip-sample distance (blue line) are shown. The activation time t_A is represented by the light gray-filled region. The inset of (a) shows the full approach (filled squares) and retraction (open squares) versus tip-sample distance H . (b) t_A is measured longer than that of (a), indicating the randomness of the activation time of the rupture. The inset is the schematic of the activation energy barrier ($\Delta\Omega$) for rupture, where W , W_0 and $\Delta\Omega_{tot}$ are the neck-width of the nanobridge, its critical width and the grand potential, respectively.	36
4.3	(a) Plot and (b) density plot of t_A versus H_r for rupture of the nanometer water bridge, which exhibits random distribution. This result shows that the rupture process follows Poisson statistics. The results are obtained under ambient conditions, RH = 35% and temperature 23.2 °C.	38

4.4	A histogram plotting the t_A at $H_r = 1.9$ and 2.5 ± 0.1 nm in Fig. 4.3 (a). This plot is obtained by the normalization by the total number of rupture events from $H_r = 1.76$ - 2.06 (a) and 2.37 - 2.67 nm (b). The t_A distribution shows the exponential decay behavior and fitted to an exponential decay (red line)	39
4.5	The rupture rate Γ as a function of H_r for temperature $T = 23.2$ (open circles) °C at RH 35%. Γ is obtained from the exponential fit for the distribution of activation time at a given H_r , as shown in Fig. 2(b). It shows that increasing the rupture distance H_r , increasing the rupture rate Γ	41
4.6	(a) The spatial distribution and (b) the rupture rate Γ as a function of H_r for different size of water nanobridge. The results are obtained on the ambient conditions, temperature $T = 26.7$ °C, and RH $37 \pm 2\%$. The each peak position of the spatial distribution in Fig. 4.5 (a) are $H_r = 1.5 \pm 0.46$ and 2.4 ± 1.06 nm. From the (a), we know that the spatial distributions have the different size of water nanobridge. The water nanobridge, which has the spatial distribution for large peak position, has the low rupture rate Γ on the rupture distance H_r [see of (b)].	43

- 4.7 The spatial distribution as a function of the rupture distance H_r at the temperature T of 20.7 (open rectangles), 23.2 (open circles), and 26.7 °C (open triangles), while RH is maintained at $37\pm 2\%$. We observed that the spatial distributions in each temperature have almost same peak position (± 0.3 nm) of the rupture distance H_r in (a). To see in detail in (a), we had normalized the P_{app} about maximum peak value of P_{app} (shown in (b)). 45
- 4.8 The rupture rate Γ as a function of the rupture distance H_r at the temperature T of 20.7 (open rectangles), 23.2 (open circles), and 26.7 °C (open triangles), while RH is maintained at $37\pm 2\%$. Γ is obtained by the exponential fit for the distribution of activation time at a given H_r , as shown in Fig. 4.5. It is observed that Γ increases as the rupture distance H_r or the temperature T increases. 46

4.9	(a) Log-scale plot of the rupture rate Γ as a function of $1/T$ at $H_r = 1.6$ (open squares), 1.9 (open circles), and 2.2 nm (open triangles). The dashed lines represent the experimental fit of the Arrhenius equation, Eq. 4.3, obtained at T of 20.7 , 23.2 and 26.7 °C and at RH of $37\pm 2\%$. (b) The energy barrier $\Delta\Omega$ is presented as a function of the rupture distance H_r , which is based on the fitting results of (a). The decrease of $\Delta\Omega$ with the increase of H_r suggests that the liquid-to-gas transition or the bridge rupture is more favorable at the larger distance.	49
4.10	Sketch of the water nanobridge formed between a tip and flat sample. θ_1 and θ_2 are the tip surface and sample surface contact angles. The nanobridge neck diameter is W	51
A.1	The time-resolved amplitude (a) and phase (b) signal near the moment of rupture of the same water nanobridge. The real-time amplitude / phase (black open circles), its time-averaged amplitude / phase (red open triangles), and the tip-sample distance (blue line) are presented as a function of time. The activation time t_A is marked by the gray-filled area.	63
B.1	(a) The apparent probability of the water nanobridge rupture as a function of the tip-sample distance. (b) The rupture rate Γ of the water nanobridge versus the tip-sample distance, as obtained from the spatial distribution of the apparent probability in (a).	66

C.1	(a) Optical curves of double-tapered and aperture NSOM probe.	
	(b) Transmittance as function of Au coating thickness of double tapered and Axicon NSOM probe.	70
C.2	(a) Time evolution of PL spectra: each time slice was averaged for 1 second. (b) Energy shifts of the peak 3, 4, and 5 for 150 seconds at an excitation power of 400 nW. The three peak traces exhibit synchronized energy fluctuations. Here the synchronous group lines are denoted as 3, 4, and 5, whereas the asynchronous peaks are denoted as 1, 2. (b) The line profile of the red dotted line (full width at half maximum (FWHM) 320nm) in (d)-(5). The line profile is fitted by a Gaussian curve to get the FWHM of the optical image, which is used to estimate the spatial resolution of the NSOM [15]. (c) Near-field images of each peak in the top of Fig. C.2(a). The image scan area is 800 nm×800 nm with a pixel size of 20 nm and the excitation power is 400nW. The crosses in Fig. C.2(c)(3)-(5) represent the center of the QD in the NSOM images.	73

C.3	[(a)-(d)] Time evolution of PL spectra showing the characteristic spectral fluctuation for different excitation powers: (a) 100nW, (b) 200nW, (c) 400nW and (d) 800nW. Two synchronous groups of emission lines are indicated by arrows 1 and 2. (e) The energy shifts in unit time (1 sec) of the brightest peak in group 2 for various excitation powers. (f) A linear fit of the standard deviation of unit time energy shifts as a function of excitation power for arrow 2 in graphs (a), (b), (c), and (d).	75
C.4	[(a)-(d)] Time-integrated spectral diffusion for applied external electric fields at an excitation power of 400nW. (a) 0V, (b) 1V, (c) 2V and (d) 3V applied bias voltage. (e) The difference of energy shifts with 1 sec integration depending on various applied bias voltages. (f) A linear fit of the standard deviation of unit time energy shifts as a function of electric field at the specified arrow position. Of note here is how the increasing electric field decreases the jitter, while increasing excitation density increases it.	77

Chapter 1

Introduction

1.1 Rupture kinetics of capillary-condensed water nanobridge

The nanometric water bridge is formed by capillary condensation between two close bodies in ambient condition, and is a commonplace phenomenon in nature. The water bridge plays an important role in the dynamic processes such as friction, adhesion and solvation, and is widely used in nanotechnology including dip-pen lithography, atomic force microscopy (AFM) and micro-electro-mechanical systems. Recently, it has been well known that the water bridge is essential in understanding the biological mechanisms of the ion-channel and protein folding. Therefore, it is important to have better and broader understanding of the mechanics, dynamics as well as kinetics of the capillary-condensed water bridge in ambient condition, from its formation to rupture.

There have been extensive studies on the formation of the capillary water nanobridges over the last several decades. In most previous theoretical studies, the Kelvin-Laplace equation has been used to determine the size and shape of the water bridge, which forms at the nanoscopic contacts of solid surfaces. In particular, if the water bridge is formed in thermodynamic equilibrium, the radius of curvature of the bridge is equal to the Kelvin radius, and thus the bridge should break up or rupture at the distance equal to twice the Kelvin radius. However, the applicability of this approach to the capillary bridge at the nanoscale is still in debate. Based on the experimental observation and theoretical model of the water bridge, Riedo *et al.* have found that the volume of the stretched water bridge is proportional to the rupture distance. Because the curvature radius of the water bridge changed during the tip retraction, the state of the water bridge is not in thermodynamic equilibrium. From the results, they found that the stretched water bridge breaks up a distance that is much larger than twice of the Kelvin radius.

In thermodynamic nonequilibrium, the rupture process of the water bridge is associated with the chemical potential gradients that may result in material transfer and trigger the irreversible bridge rupture. Thus, the Kelvin equation is not applicable in thermodynamic nonequilibrium. Men *et al.* [9] applied the density functional theory, which is based on the energy barrier, in order to study the rupture process of the water bridge. Their work demonstrated the origin of the hysteresis behavior in the formation and rupture of the water bridge, and the rupture started by overcoming the energy barrier, which is so called the

thermal activation process.

Despite the established theoretical results, however, experimental works on the kinetics of the nanoscale rupture process in terms of thermal activation still lack, unlike the well studied capillary formation. In this Letter, we directly measure the activation time needed for the water bridge to be ruptured by using the quartz-tuning-fork (QTF) based AFM in ambient condition. We find that the activation time obtained at the various rupture distance exhibits random distribution and shows the characteristic exponential decay, which indicates that the rupture process follows the Poisson statistics, which is typical of the thermal activation processes. We also have measured the dependence of the rupture rate on the tip-sample distance as well as the temperature, from which we can estimate the values of the activation energy.

1.2 Time-resolved dynamic force microscopy by QTF based AFM

Imaging individual atoms was an elusive goal until the introduction of the scanning tunneling microscope (STM) in 1981 by Binnig, Rohrer, Gerber, and Weibel (1982) [1]. This humble (1982). This humble instrument has provided a breakthrough in our ability to investigate matter on the atomic scale: for the first time, the individual surface atoms of flat samples could be made visible in real space. Despite the phenomenal success of the STM, it has a serious limitation. It requires electrical conduction of the sample material, because

it uses the tunneling current which flows between a biased tip and a sample. Atomic force microscopy (AFM) could ultimately achieve true atomic resolution because of measured significant forces between single atoms. Also, AFM can image virtually any flat solid surface without the need for surface preparation because electrical conductivity of the sample is not required. Since its development in 1982 by Binnig, many experimental studies on nanoscale phenomena have utilized AFM to image the atomic topography and measure interacting forces [2, 3].

In order to measure the force between a small tip and a sample, a tiny probe called a cantilever is employed. There are various methods for detecting the motion of the cantilever with nanometer scale accuracy. The water nanobridge formed by capillary condensation between two closely spaced bodies in ambient condition. The water nanobridge has important implications for the recently discovered phenomenon of dip-pen nanolithography (DPN) [4, 5]. By using AFM, theoretical investigations provided to understand the water nanobridge. The interaction force between two solids mediated by liquid bridge was studied by Bhushan *et al.* [6, 7]. Jang *et al.* Has studied the capillary force and meniscus structure as a function of tip-sample distance by using Molecular theories, including molecular dynamics and Monte Carlo simulations [8]. Men *et al.* were investigated the formation and rupture process of liquid bridges by lattice density functional theory [9]. Experimental studies of the water nanobridge lack less than theoretical ones because it is difficult manipulating the water nanobridge using the cantilever-based AFM due to its mechanical instability.

To overcome the mechanical instability, called jump-to-contact, a quartz tuning-fork (QTF) based AFM is investigated which can be manipulated the stable water nanobridge [10]. Using QTF-AFM, an unusual stepwise decrease of the force gradient associated with the water nanobridge is observed during its stretch. Such elasticity is indicative of an atomic-scale stick-slip at the tip-water interface [10]. By using amplitude-modulation QTF-AFM, it measured quantitative values of the elasticity, viscosity and dissipation energy of the water nanobridge [11].

In the experimental studied using QTF-AFM, there have been many studies of the quantitative measurements of the water nanobridge over the last decades. However it is still lack of the kinetics of water nanobridge, such as formation and rupture process. In particular, it is well-known that the formation and rupture process of water nanobridge is originated from the thermal activation process by many theoretical studies [9, 12]. To study about this processes, it is required a novel tool which detect the temporal changes of the interaction exerted on the tip. Thus it is employed the time-resolved dynamic force microscopy (TRDFM). By using TRDFM, we can expect to be a novel platform for microscope for studies of dynamic process of liquid system.

1.3 Outline of this thesis

The focus of this thesis is rupture kinetics of water nanobridge using TRDFM, which is based on QTF-AFM.

In chapter 2, we will introduce the quartz tuning-fork which is important part of TRDFM operation improved QTF-AFM. The quartz tuning-fork, unlike the cantilever, has the characteristics of self-sensing, high stability and high sensitivity. These advantages prevent the jump-to-contact for tip approaching in nanoscale, and provide to study the mechanical property of liquid by capillary condensation.

In chapter 3, we will represent the water nanobridge characteristics by capillary condensation in nanoscale by using QTF-AFM

In chapter 4, we observed the real time at break up of water nanobridge using TRDFM. By statistical analysis, we obtained that the rupture process is associated with the activated process and is related to temperature dependence. Also, we confirm that the dependence of the rupture rate on the various temperatures is related to activation energy barrier height.

Bibliography

- [1] G. Binnig, H. Rohrer, Ch. Gerber, and E. Weibel, *Phys. Rev. Lett.* **49**, 57 (1982).
- [2] R. García, and R. Pérez, *Surf. Sci. Rep.* **47**, 197 (2002).
- [3] F. J. Giessibl, *Rev. Mod. Phys.* **75**, 949 (2003).
- [4] R. D. Piner, J. Zhu, F. Xu, S. Hong, and C. A. Mirkin, *Science* **283**, 661 (1999).
- [5] S. Hong, and C. A. Mirkin, *Science* **288**, 1808 (2000).
- [6] R. Stifter, O. Marti, and B. Bhushan, *Phys. Rev. B* **62**, 13667 (2000).
- [7] S. Cai, and B. Bhushan, *Nanotechnology* **18**, 465704 (2007).
- [8] J. Jang, G. C. Schatz, and M. A. Ratner, *J. Chem. Phys.* **120**, 1157 (2004).
- [9] Y. Men, X. Zhang, and W. Wang, *J. Chem. Phys.* **131**, 184702 (2009).
- [10] H. Choe, M. -H. Hong, Y. Seo, K. Lee, G. Kim, Y. Cho, J. Ihm, and W. Jhe, *Phys. Rev. Lett.* **95**, 187801 (2005).

- [11] M. Lee, B. Sung, N. Hashemi, and W. Jhe, *Faraday. Disc.* **141**, 415 (2009).
- [12] E. Sahagún, P. García-Mochales, G. M. Sacha, and J. J. Sáenz, *Phys. Rev. Lett.* **98**, 176106 (2007).

Chapter 2

Quartz Tuning-Fork for Force Measurement

2.1 Introduction

AFM is widely used to obtain the atomic resolution [1], and force measurement for solid surface [2]. AFM is investigated to observe the adsorbed water layer at solid surface [3,4] and the mechanical properties of the confined water between solid and solid surface [5,6], is applied to study various water system. In particular, the water nanobridge by capillary condensation is widely studied because of applicability in nanotechnology.

However, the water nanobridge in solid-solid surface is occurred the mechanical instability by capillary force. To investigate the dynamic process of the water nanobridge, it need to constant tip-sample distance, but it is difficult

to work in ambient condition owing to thermal drift.

To investigate the water nanobridge, we need to the constant tip-sample distance, to avoid the mechanical instability and the sensitive detection as force sensor. The quartz tuning-fork is the high stiffness compared with the cantilever. But it has less sensitive than about temperature changes, the high sensitivity.

In this chapter, the quartz tuning-fork as AFM quantitative force sensor will introduce.

2.2 Electrical Driven Quartz Tuning-Fork

Quartz tuning-fork (QTF) consists of two prongs with piezoelectric quartz crystal. Each prongs is attached metal plate electrode, as shown Fig. If the metal electrode at each prongs of QTF is applied bias AC voltage, each prongs occur deflection by piezoelectric effect. Based on this mechanism, deflection of QTF prong represents the interaction change at QTF prong. In general, the operation methods of QTF is as follows: electrical modulation, mechanical modulation.

Mechanical modulation measures the electrical QTF signal for mechanical oscillation of a prong of the QTF. Electrical modulation measures the electrical signal change of another prong which caused by AC signal driving of one prong of the QTF. The electrical modulation is equivalent to as RLC circuit which based on the simple harmonic oscillation model, as shown below.

$$L\ddot{q} + R\dot{q} + \frac{1}{C}q = V_d e^{i\omega_d t} \quad (2.1)$$

with

$$\omega_d = 2\pi f_0 = \frac{1}{\sqrt{LC}}, \quad Q = \frac{1}{R} \sqrt{\frac{L}{C}} \quad (2.2)$$

where V_0 is the driving voltage, ω_d is the angular frequency, q is the charge, ω_0 is the resonance frequency and Q is the quality factor.

The electrical modulation is advantages of self-actuating and sensing. But, it is occurred the parasitic capacitance by AC voltage driving. The parasitic capacitance is resulted in that the electrical modulation QTF is equivalent to RLC circuit, called by Butterworth-von Dyke equivalent circuit [7–9].

The different between electrical output (apparent signal) and output signal of RLC circuit (actual signal) QTF is as follow in Fig. 2.1(b)

In Fig. 2.1(b) , we can induce the QTF output amplitude / phase relation in both apparent and actual signal from electrical driven QTF.

$$A_m = \sqrt{A_e^2 - 2A_e A_C \sin(\theta_0 + \theta_e) + A_C^2}, \quad (2.3)$$

$$\theta_m = \tan^{-1} \left[\frac{A_e \sin(\theta_0 + \theta_e) - A_C}{A_e \cos(\theta_0 + \theta_e)} \right]. \quad (2.4)$$

From eq. 2.3 and 2.4 , we can the correction of QTF output signal from the electrical modulation, as shown Fig.2.2.

From these results, we can compensate to the output signal of the electrical modulation QTF using the relation between apparent and actual output signal.

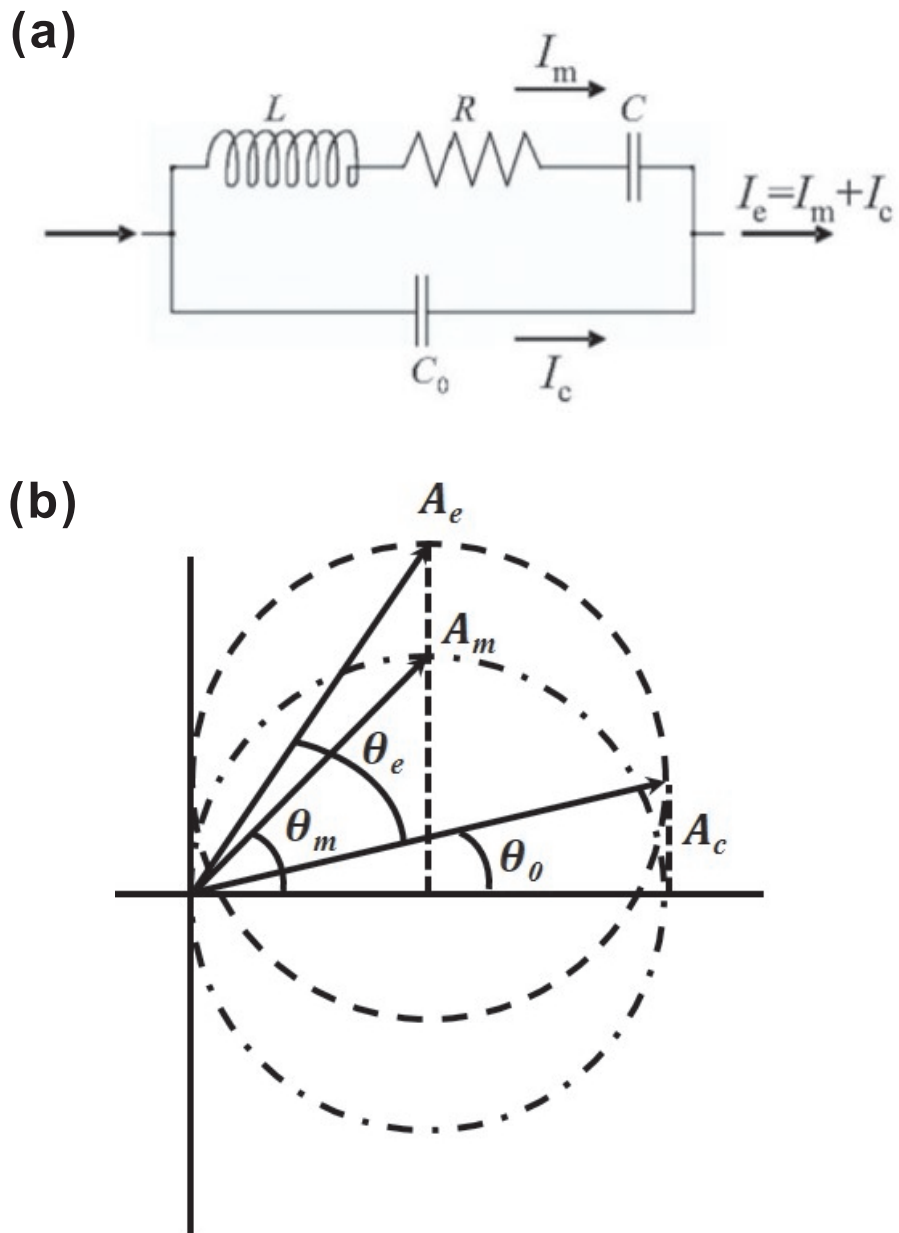


Figure 2.1: (a) Schematic of RLC circuit model for electrical modulation QTF. (b) Geometrical interpretation of electrical modulation QTF is depicted. The circle (dot-and-dash line) is shifted along the y-axis as much as A_c

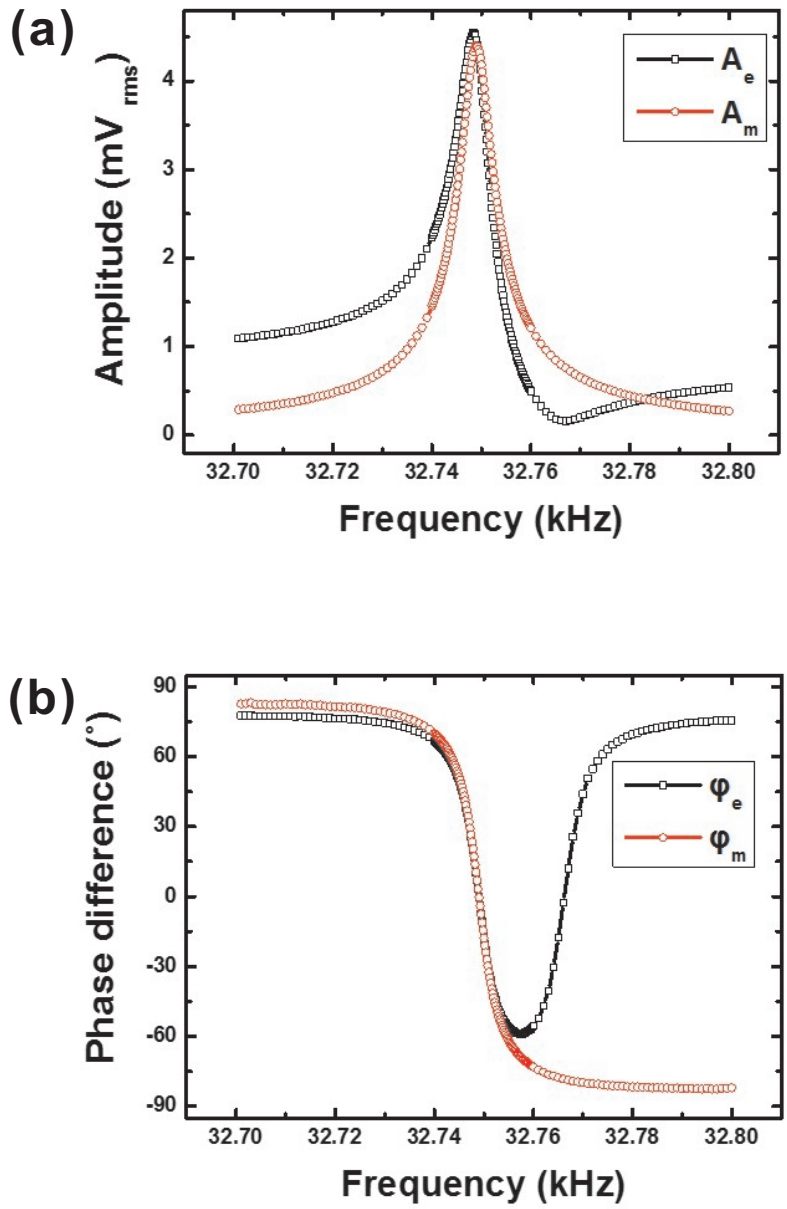


Figure 2.2: Comparison of apparent signal (open squares) and actual signal (open circles) in electrical modulation QTF, (a) amplitude. (b) of phase difference.

2.3 Mechanical Oscillation Amplitude of QTF

As the QTF operate by the electrical modulation, we do not know exactly how about QTF prong oscillation amplitude is. This problem can be solved by measuring piezoelectric coupling constant α . Piezoelectric coupling constant is the ratio of the charge induced by piezoelectric effect and the deflection of a prong of QTF. It has been known that the charge q is proportional to the deflection x in many studies [1, 7, 10]. In addition, the output current I_{rms} was also observed to be linearly proportional to the deflection x , as checked by an optical microscope [10]. with these results, if the piezoelectric coupling constant α and the I-V gain Z_G are known, the deflection x can be derived from V_{out} , the output voltage of QTF read by the lock-in amplifier. V_{out} which is induced by the rms deflection x_{rms} of the QTF, can be expressed by

$$V_{out} = Z_G \cdot I_{rms} = Z_G \omega_d \alpha x_{rms}, \quad (2.5)$$

When the QTF is driven with a voltage amplitude V_d at the resonance frequency ω_0 , V_{out} is also written as

$$V_{out} = Z_G \frac{V_d}{R} = Z_G Q \omega_0 C V_d, \quad (2.6)$$

which is obtained by using the equivalent RLC series circuit model. From equations eq. 2.5. and eq. 2.6, the relation between x_{rms} and V_d is then

$$x_{rms} = \frac{V_{out}}{Z_G \omega_d \alpha} = \frac{QC}{\alpha} V_d. \quad (2.7)$$

By these methods, we can obtain the mechanical oscillation amplitude of QTF prong. In our experiment, x_{rms} is as follow, based on QTF specification.

2.4 Electrical modulation QTF as a Force Sensor

Because of using the electrical modulation QTF as force sensor, electrical oscillation QTF signal is needed to convert the mechanical oscillation QTF signal. Eq.2.8 can be obtained from alpha in the previous chapter 2-2 as

$$(L\alpha)\ddot{x} + (R\alpha)\dot{x} + \left(\frac{\alpha}{C}\right)x = V_d e^{i\omega t}, \quad (2.8)$$

which has the same form of equation of motion as the simple harmonic oscillator,

$$m_{eff}\ddot{x} + b_{eff}\dot{x} + k_{eff}x = F_{eff}e^{i\omega t}, \quad (2.9)$$

where m_{eff} , b_{eff} and k_{eff} denote the effective mass, damping coefficient and stiffness of the QTF, respectively, and F_{eff} the effective force exerted on the QTF. in addition, the resonance frequency ω_0 and quality factor Q are

$$\omega_0 = \sqrt{\frac{k_{eff}}{m_{eff}}}, \quad Q = \frac{\sqrt{m_{eff}k_{eff}}}{b_{eff}}. \quad (2.10)$$

To get the response of the QTF to an external force exerted, we consider the equation of motion in free oscillation. The equation of motion at free oscillating QTF with driving force F_0 is obtained as,

$$m_{eff}\ddot{x}^{(0)} + b_{eff}\dot{x}^{(0)} + k_{eff}x^{(0)} = F_{eff}e^{i\omega t}. \quad (2.11)$$

and the displacement at free oscillation $x^0(t)$ can be written as $x^0(t) = A_0 e^{i(\omega_d t + \varphi)}$ where A_0 is the amplitude of free oscillation and φ is the phase difference between the driving force and the displacement. When the driving frequency is equal to the resonance frequency, i.e., $\omega_d = \omega_0$, then $\varphi = -\frac{\pi}{2}$. If an interaction force F_{int} is exerted on the force sensor, the equation of motion becomes

$$m_{eff}\ddot{x} + b_{eff}\dot{x} + k_{eff}x = F_{eff}e^{i\omega_d t} + F_{int}, \quad (2.12)$$

and the displacement $x(t)$ in the presence of interaction is expressed by $x(t) = A e^{i\theta} e^{i(\omega_d t + \varphi)}$ where A is the amplitude in the presence of interaction and θ is the difference between the phases with and without the interaction. It is usually assumed that $F_{int} = -b_{int}\dot{x} - k_{int}x$ if the amplitude is small compared to the characteristic length of interaction [5,9,11] (here the subscript ‘int’ denotes the response to the interaction exerted on the QTF). For the water nanobridge, it can be extended to the mass, i.e.,

$$F_{int} = -m_{int}\ddot{x} - b_{int}\dot{x} - k_{int}x. \quad (2.13)$$

Inserting eq. 2.13 into eq. 2.12 and subtracting eq. 2.11 from eq. 2.12 to eliminate F_{eff} yields

$$-m_{int}\omega_d^2 + \iota b_{int}\omega_d + k_{int} = (-m_{eff}\omega_d^2 + \iota b_{eff}\omega_d + k_{eff}) \cdot f(A, \theta), \quad (2.14)$$

where

$$f(A, \theta) = \left(\frac{A_0}{A} \cos \theta - 1 \right) + \iota \left(-\frac{A_0}{A} \sin \theta \right). \quad (2.15)$$

Comparing the real and imaginary parts on both sides, two equations for k_{int} , m_{int} and b_{int} can be obtained:

$$k_{int} = k_{eff} \left[\left(\frac{A_0}{A} \cos \theta - 1 \right) \left(1 - \frac{\omega_d^2}{\omega_0^2} \right) + \frac{\omega_d}{Q\omega_0} \frac{A_0}{A} \sin \theta \right], \quad (2.16)$$

$$b_{int} = \frac{k_{eff}}{\omega_d} \left[\frac{\omega_d}{Q\omega_0} \left(\frac{A_0}{A} \cos \theta - 1 \right) - \frac{A_0}{A} \sin \theta \left(1 - \frac{\omega_d^2}{\omega_0^2} \right) \right]. \quad (2.17)$$

Thus, we can obtain the interaction stiffness k_{int} and the damping coefficient b_{int} from the external interaction by measuring the amplitude and phase difference signals.

2.5 Conclusion

We present the characteristic of quantitative QTF as force sensor. To use electrical modulation QTF model, we can obtain the compensated parasitic capacitance by formula. From these results, the interaction force at QTF one prong can be obtained by the electrical modulation QTF output signal, and we obtain basic step for the quantitative analysis of the water nanobridge.

Bibliography

- [1] F. J. Giessibl, *Appl. Phys. Lett.* **76**, 1470 (2000).
- [2] K. Karrai and I. Tiemann, *Phys. Rev. B* **62**, 13174 (2000).
- [3] J. Hu, X-D. Xiao, and M. Salmeron, *Appl. Phys. Lett.* **67**, 476 (1995).
- [4] P. B. Miranda, L. Xu, Y. R. Shen, and M. Salmeron, *Phys. Rev. Lett.* **81**, 5876 (1998).
- [5] S. Jeffery, P. M. Hoffmann, J. B. Pethica, C. Ramanujan, H. Ö. Özer, and A. Oral, *Phys. Rev. B* **70**, 054114 (2004).
- [6] T-D. Li, J. Gao, r. Szoszkiewicz, U. Landman, and E Riedo, *Phys. Rev. B* **75**, 115415 (2007).
- [7] J. Ryche, T. Ihn, P. Studerus, A. Herrmann, K. Ensslin, H. J. Hug, P. J. A. Van Schendel, and J. J. Güntherodt, *Rev. Sci. Instrum.* **71**, 1695 (2000).
- [8] Y. Qin, and R. Reifenberger, *Rev. Sci. Instrum.* **78**, 063704 (2007).
- [9] M. Lee, J. Jahng, K. Kim and W. Jhe, *Appl. Phys. Lett.* **91**, 023117 (2007).

- [10] A. Castellanos-Gomez, N Agraït, and G. Rubio-Bollinger, *Natnotechnology* **20**, 215502 (2009).
- [11] M. Lee, and W. Jhe, *Phys. Rev. Lett.* **97**, 036104 (2006).

Chapter 3

Mechanical study of water nanobridge using QTF-AFM

3.1 Introduction

AFM has been used to investigate the water system of various type, such as interfacial water, confined nanopore water, and water nanobridge. In the case of water nanobridge by using cantilever-based AFM, the cantilever hardly support by capillary force in nanoscale, because low stiffness. It indicates that the cantilever-based AFM is difficult to manipulate the water nanobridge.

To study of water nanobridge, we need to the force sensor in AFM which satisfy to several condition as follows. (1) To avoid the mechanical instability, the force sensor should be the high stiffness. (2) To detect the small change of interaction force, the force sensor should be the high sensitivity.

In previous chapter, we presented that QTF is suitable to study of water nanobridge. It also allows a self-sensing due to its piezoelectricity, without any optical device which process to the sample or water nanobridge. In this chapter, we introduce that how QTF-AFM can measure the mechanical property of water nanobridge. In experimental results, we will obtain the elasticity and viscosity of water nanobridge.

3.2 Quartz Tuning-Fork based Atomic Force Microscopy

Our home-made amplitude modulation QTF-AFM has a high effective stiffness and a high quality factor. Thus, our set-up can avoid the mechanical instability which is originated from the interacting force between the tip and the sample surface.

Fig. 3.1 is the optical microscope image of QTF-AFM tip. We operated shear-mode AFM, which can work that the tip is oscillated parallel to the sample. In the tapping-mode operation, we could be confused with the understanding for obtained experimental data. Because we could hardly know what is the tip affected by the interaction force, such as electrostatic force, Van der Waals force, and capillary force. Also, we concern the tip and sample deformation by contact damage with the sample and tip in investigated for nanobridge.

Tip is silicon cantilever tip (CSG10, NT-MDT), has the curvature radius of 10 nm. The tip attached by epoxy at one prong of QTF, has the lateral

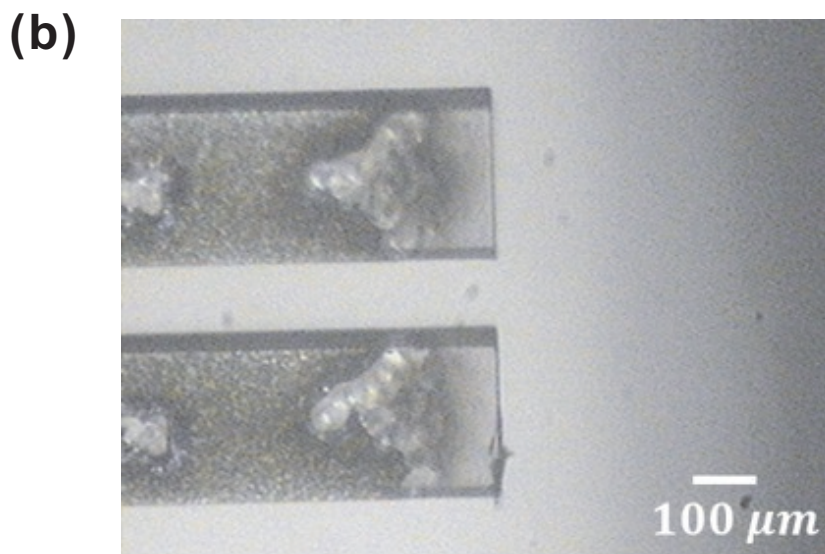
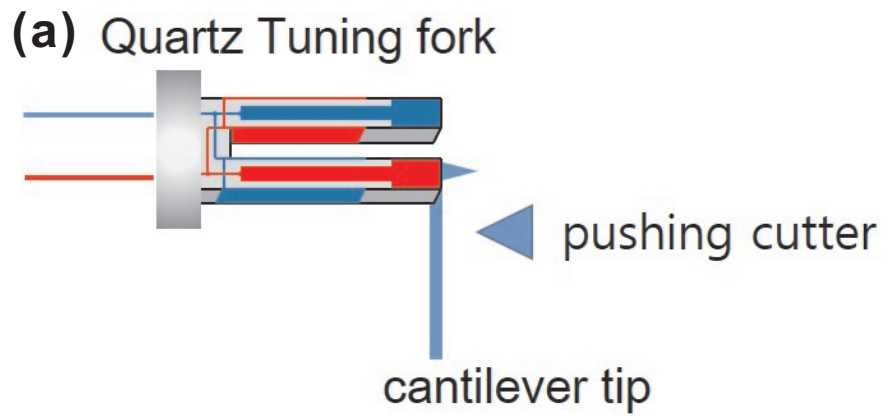


Figure 3.1: The fabricated probe tip for QTF-AFM (a) Schematic of fabrication of the probe tip for the QTF-AFM. The silicon cantilever tip attached by epoxy at one prong of QTF. (b) Optical microscope image of the glued & cut probe tip for QTF-AFM.

oscillation. The QTF (C-002RX, Epson-Toyocom Corp.) has the effective stiffness k_e of 3350 N/m, and quality factor Q of 5100. Sample is muscovite mica (Grade V-1, SPC Chem.). The mica was cleaved using an adhesive tape, sufficient rinsed by dilute acetic acid to exchange potassium ions for hydrogen ions on the cleaved surface [1], washed with deionized water and then dried with nitrogen gas.

The tip, sample and piezoelectric tube (PZT, Physik Instrumente) were contained in an air-tight acrylic chamber. In preparation of the experiment, the chamber was regulated by injecting nitrogen that contains deionized water vapor. The relative humidity was continuously monitored by a sensor (SHT75, Sensirion, specified accuracy <1.8%), placed at 2 cm away from the sample.

Figure. 3.2 shows a schematic diagram of the shear-mode QTF-AFM, which the tip is oscillating parallel to the sample surface and can measure to the lateral force. QTF one prong is driven by a function generator (Agilent, 33120A). QTF another prong detected the electrical signal change by measurement of a lock-in amplifier (EG&G, 7265), which is the interaction force between cantilever tip and sample. PC computer summarized the output signal for QTF another prong, is directly connected with the piezo electric transducer (PZT) and lock-in amplifier. Based on the output signal for QTF, it is worked the PZT for controlled the tip-sample distance.

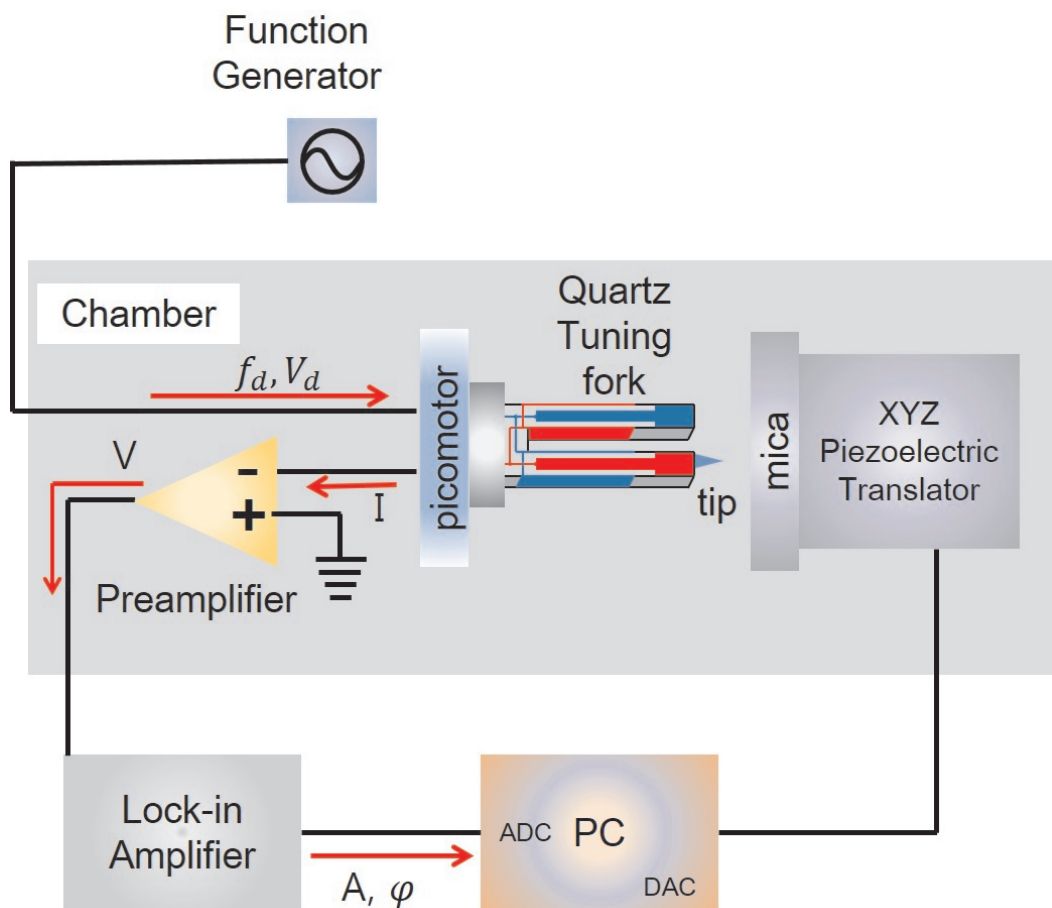


Figure 3.2: Schematic diagram of the shear-mode QTF-AFM.

3.3 Measurement of Mechanical Properties of water nanobridge

Full curves of the amplitude and phase of the probe tip during its approach and retraction are presented in Fig. 3.3 as a function of the tip-sample distance H .

During tip approach-retraction, we can be divided to four regions by nanometer water nanobridge state. When H is larger than H_r (Region A), it is not exist any difference at approach-retraction curve. It indicates that the tip experience free oscillation, so the nanometer water nanobridge is absent.

While the tip is free oscillation during approach, the water nanobridge is exist during retraction at $H_f < H < H_r$ (Region B). Thus this region has two states which have each local minimum differentiate from the energy barrier height in the grand potential. One state at the lowest energy minimum is the stable state, the other one at the higher energy minimum is the metastable state. The energy barriers of formation and rupture defined to the energy needed to overcome to form, to break the water nanobridge. In region B, we can identify that H_r is larger than H_f because the energy barrier of rupture is lower than the formation as increasing tip-sample distance.

In $0 < H < H_f$ (Region C), there has almost behavior of approach-retraction curves. At $H = H_f$, the amplitude and phase value of tip have dramatic change, this distance is the point of forming water nanobridge. After the water nanobridge formation, the amplitude / phase value of tip decrease / increase which indicates growth of the water nanobridge. As the tip approach

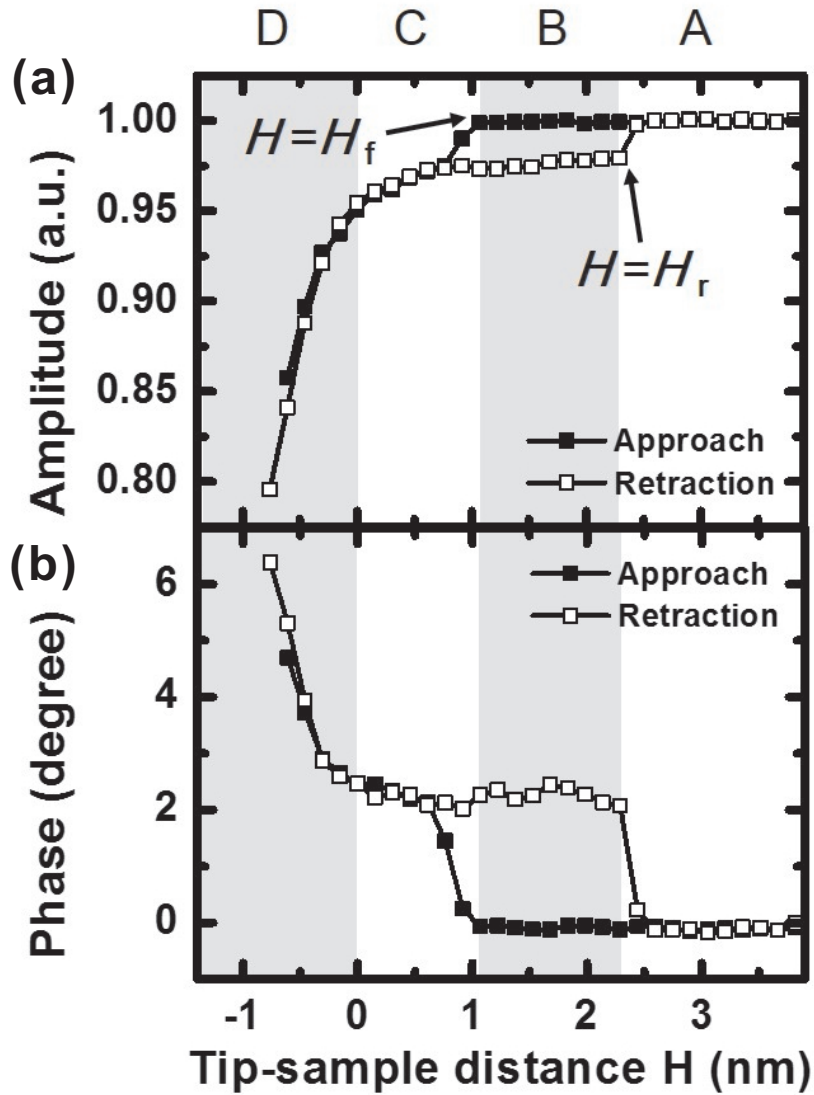


Figure 3.3: Full approach-retraction curves by the QTF-AFM (a), (b) Approach (closed squares) / retraction (open squares) curves of the measured amplitude and phase difference as a function of the tip-sample distance H . The relative humidity and temperature are maintained at 37 % and 19.7 °C. From change of the amplitude and phase difference of the probe tip, we can define to the formation, rupture distance and contact point of water nanobridge, as denoted by H_f , H_r and $H = 0$. The four regions (marked by A, B, C and D) with respect to H show the different states associated with the water nanobridge.

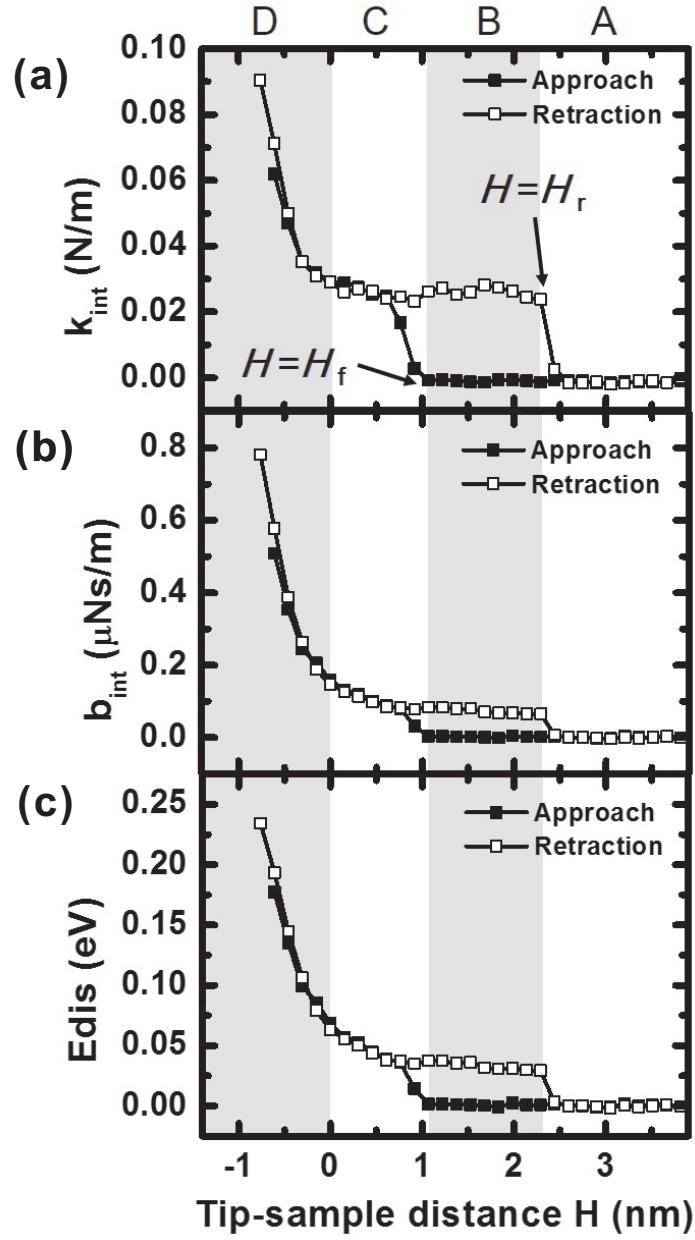


Figure 3.4: Mechanical properties of water nanobridge by QTF-AFM. (a) Interaction stiffness k_{int} , (b) damping coefficient b_{int} and (c) energy dissipation E_{diss} . Mechanical properties can be obtained from the amplitude and phase difference results in Fig. 3.3.

closer to sample (Region D), it found that the amplitude and phase value change, which indicates that the tip contact with the sample. We defined as the contact point ($H = 0$) where the slope of amplitude and phase have steep curves. These facts are study by many theoretical, experimental analyses. From this result, formation and rupture distances of water nanobridge have different values. We can understand the formation and rupture in approach-retraction curves.

We are able to obtain the quantitative values of the mechanical properties of the water nanobridge by using the previous chapter, chapter 2. Figure 3.4 show the mechanical properties (interaction stiffness, damping coefficient and energy dissipation) as a function of the tip-sample distance. The interaction stiffness (k_{int}) is the lateral stiffness experienced by the tip-sample interaction force. The damping coefficient (b_{int}) come from the viscosity property of the water nanobridge, is related to the dissipated energy per oscillation, $E_{diss} = \pi b_{int} \omega A^2$ (ω is the driving frequency of QTF). The energy dissipation (E_{diss}) could be calculated the hysteresis during one period of the QTF motion [2] resulting from the friction at the nanoscale [3].

Notice that the mechanical contact position between the tip and the sample was determined to be the point at which the tip experiences a drastic change of the interaction stiffness k_{int} in the closed sample surface. This point indicates that the tip begins to sense the solid-liquid interaction. When mica surface is exposed to in the air, we expect to the case without the water nanobridge between tip and sample. In this case, the tip experiences a drastic increasing of the interaction stiffness k_{int} without the hysteresis loop. In comparisons be-

tween with and without the water nanobridge by the capillary condensation, we can verify whether or not the existence of water nanobridge, define the contact point $H = 0$ and rupture distance H_r .

3.4 Conclusion

In this chapter, we have demonstrated the QTF-AFM which is suitable to study the water nanobridge in the capillary force region. The QTF-AFM allows the stable approach-retraction curves and manipulation of the water nanobridge, thus it can be analyzed the quantitative measurement of water nanobridge.

Bibliography

- [1] T. E. Balmer, H. K. Christenson, N. D. Spencer, and M. Heuberger, *Langmuir* **24**, 1566 (2008).
- [2] M. Lee, and W. Jhe, *Phys. Rev. Lett.* **97**, 036104 (2006).
- [3] R. Szoszkiewicz, E. Riedo, *Phys. Rev. Lett.* **95**, 135502 (2005)

Chapter 4

Rupture Process of water nanobridge¹

4.1 Introduction

Rupture process of nanometer water bridge, is formed and disappeared between two surfaces, is still poorly understood, though its plays an important role in nano-imaging and nano-fabrication.

In this chapter, we introduce the time-resolved dynamic force microscopy for studies of temporal-changing of water nanobridge. We report the real-time observation of rupture process of a nanometer water nanobridge which formed between tip and surface. During tip pulling, we measured the activation time that is latency time at break up of nanometer water nanobridge. By statistical

¹This chapter was modified and rewritten on the basis of the work which was accepted to *Appl. Phys. Lett.* (2014)

analysis, we obtained that the distribution of activation time of each rupture distance have an exponential decay behavior. The experimental results present that the rupture process is associated with the activated process and follows the Poisson statistics. Also, we confirm that the dependence of the rupture rate on the temperature agrees with the Arrhenius law is related to activation energy barrier in rupture process. It inform that the activation energy barrier is an important key for the rupture event of nanometer water nanobridge.

4.2 Activation Process associated with Rupture of water nanobridge

4.2.1 Time-Resolved Dynamic Force Microscopy

To study of rupture process in water nanobridge, it is required to measure the temporal signals of the interaction applied on the probe tip during the pulling tip. Thus, we employed the time-resolved dynamic force microscopy (TRDFM) by using a field-programmable gate array (PXI – 7833R, National Instrument), which carry out the measurement intervals short enough to detect the transient behaviors with an error of about 1 μ s. TRDFM controls the tip-sample distance at a fixed value and measures all the temporal variations of the force as a function of the distance and time. It enables one to observe the time-domain changes of the interaction exerted on the force sensor.

The experimental materials are equal to that in the previous chapter. For

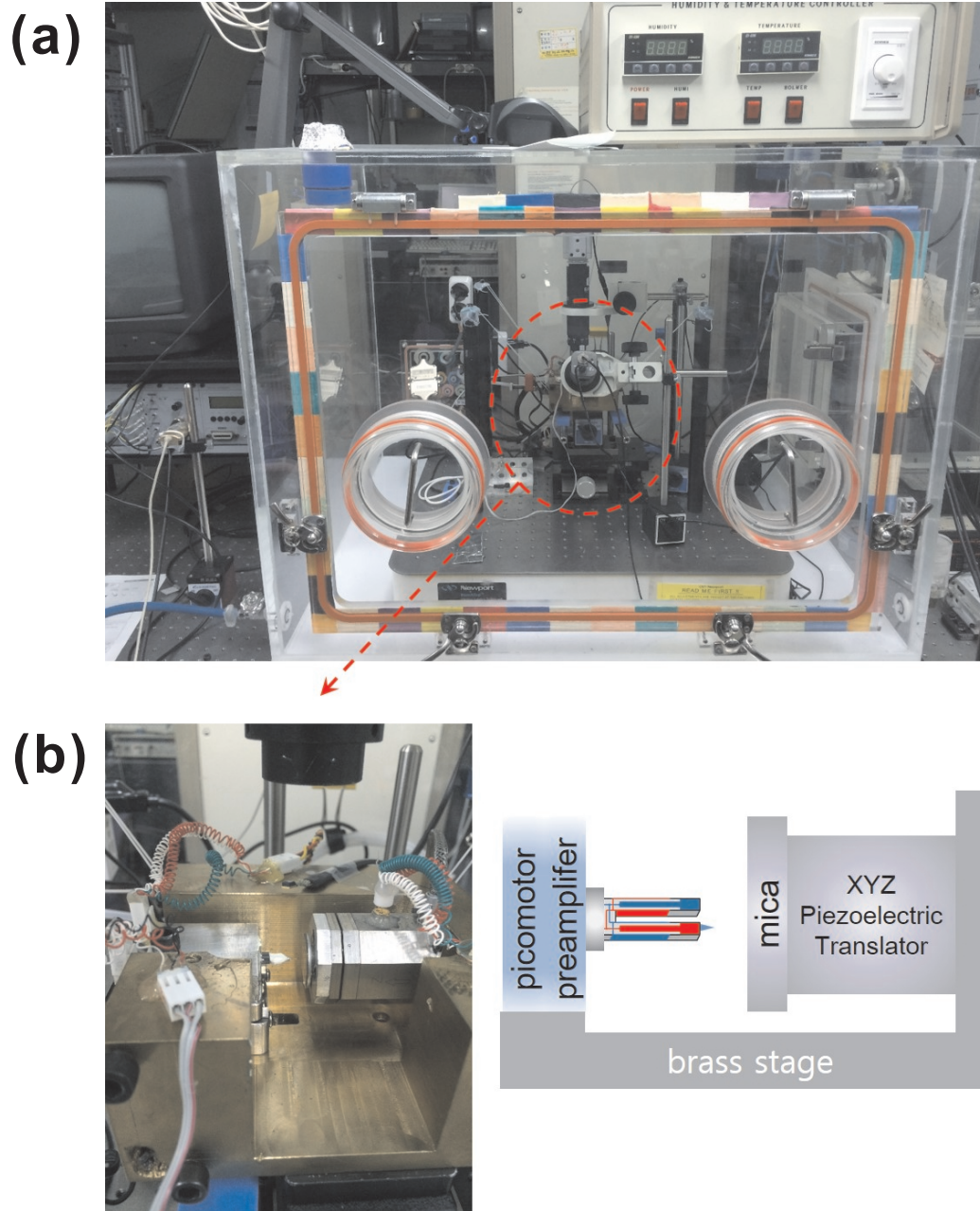


Figure 4.1: Time-resolved dynamic force microscopy (TRDFM) system. (a) The experimental system in the humidity-controlled air-tight chamber. (b) The part is focused the brass stage of the TRDFM, which is consist of the QTF probe tip and mica sample and PZT. The one-bode brass stage reduced the thermal drift speed.

the probe tip, we used the sharp silicon cantilever tip (CSG10, NT-MT) whose nominal radius of curvature is 10 nm. It was attached to the end of one prong of the quartz tuning-fork (QTF) to oscillate in the lateral direction in the vicinity of the sample. The resonance frequency of probe tip was about 32 kHz and the quality factor Q was about 5100. The root-mean-square (rms) amplitude for the free oscillation of the probe tip was 0.34 nm.

The atomically flat muscovite mica (Grade V-1, SPI Chem) was used for the sample, which was cleaved and rinsed with the dilute acetic acid of 0.87 M concentration and washed by deionized water. The experimental system was placed in a humidity and temperature control chamber.

Notice that the thermal drift during the experiment is suppressed by the simple and compact apparatus of experiment, the air-tight acrylic chamber, and the isothermal-isohumidity control facility, as presented in Fig. 4.1. Therefore, the thermal drift was less than 20 pm/s, thus it is negligibly small and can be systematically compensated.

4.2.2 Rupture rate of water nanobridge

Typical curves of the amplitude of the probe tip during its approach and retraction are presented in the inset of Fig. 4.2(a) as a function of the tip-sample distance H . During tip approach-retraction, we can be divided to some regions by nanometer water nanobridge state. We focus at $H = H_r$ as break up the water nanobridge [1]. From change of the amplitude and phase of the probe tip, we can define to the formation position, rupture distance and contact point

of water nanobridge, as denoted by rupture distance = H_r in Fig. 4.2. These facts are study by many theoretical, experimental analyses [2]. From this result, we inform that the formation and rupture distances of water nanobridge have different values. We can understand the rupture in approach-retraction curves.

To study the rupture process of water nanobridge, we investigated the AFM signals relative to measurement time in rupture point of water nanobridge, $H = H_r$. Figures 4.2 is the tip oscillation amplitude and tip-sample distance with respect to measurement time as rupture of water nanobridge at the relative humidity (RH) 35% and temperature 23.2 °C. The sample move far tip like as stepwise discrete retract (blue line) with the step size of 0.15 *nm* and staying time of 0.5 sec. The measurement of phase (open circles) are at 10 *ms* as shown in Fig. 4.2. Due to thermal drift during the measuring oscillation phase is less than 20 *pm/s*, the measuring experimental data obtained a point of sample at every approach-retraction cycle [3].

Fig. 4.2 are the time-resolved AFM signals at the close rupture point (at $H = H_r$) of water bridge. At $H < H_r$, we observed the stable formed water nanobridge since the measured phase data have the low fluctuation value and plus values. We observe several phenomena in the phase change of probe tip before water nanobridge snapping: (i) the phase fall does not occur instantly, but a little later during each stepwise retraction, indicated by t_A (we call the activation time), (ii) the activation time t_A have the randomly distribution for each rupture distance H_r . It infer that t_A have various values in the same experimental conditions [Fig. 4.2 (a), (b)], is associated with the rupture process

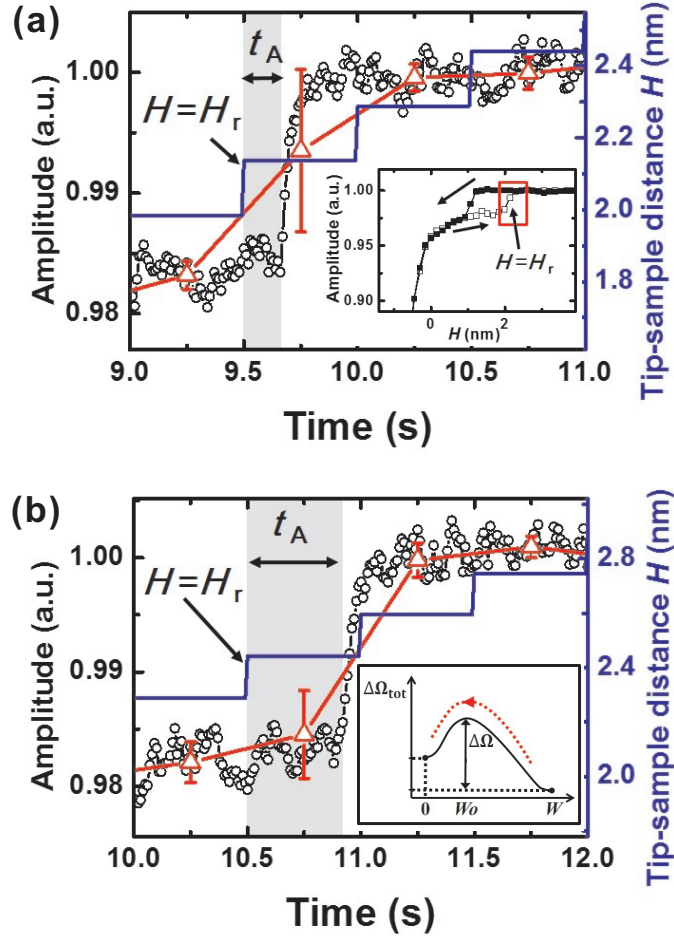


Figure 4.2: The time-resolved AFM amplitude signals near the moment of rupture of the water nanobridge. The relative humidity and temperature are maintained at 35% and 23.2 °C. (a) The oscillation amplitude of the probe tip (open circles), its time-averaged phase (red triangles) and the stepwise change of the tip-sample distance (blue line) are shown. The activation time t_A is represented by the light gray-filled region. The inset of (a) shows the full approach (filled squares) and retraction (open squares) versus tip-sample distance H . (b) t_A is measured longer than that of (a), indicating the randomness of the activation time of the rupture. The inset is the schematic of the activation energy barrier ($\Delta\Omega$) for rupture, where W , W_0 and $\Delta\Omega_{tot}$ are the neck-width of the nanobridge, its critical width and the grand potential, respectively.

of water nanobridge.

We concentrated on the t_A which have the randomly value. To statistical analysis of the activation time, we have the approach-retraction cycles more than a thousand times, and each of the three approach-retraction cycles moved to 100 nm along the sample surface from the previous position surface. This works act to avoid the position dependence and to get the thermal drift. We obtained the t_A versus H_r recording at each approach- retraction cycle, as shown in Fig. 4.3.

Figure 4.3 is recorded by the experiment data of t_A and H_r at each approach-retraction cycle. In Fig. 4.3 (a), we observed that the distribution t_A with respect to H_r is spread out, but have the some overlapped datas. In Fig. 4.3, we see that the number of the data point is less than 1000. From the density plot for Fig. 4.3 (a), we know that how much the overlapped data number, as see in Fig. 4.3 (b). The overlapped data is obtained in neither same the sample positon nor same tip-sample distance. Because the arbitrary data position separated from the previous data position by 100 nm. In Fig. 4.3, we see that the longer t_A is decreasing number of activation time for the same H_r . After breakup of the water nanobridge at certain distance, it should not be ruptured again at the same tip-sample distance. In other words, once the water nanobridge snapped off at a certain distance, the rupture distance of water nanobridge has the different value even if probe tip is retracted on surface again. Thus, the each rupture process of water nanobridge is the independent events, can be considered as the Poisson Statistics.

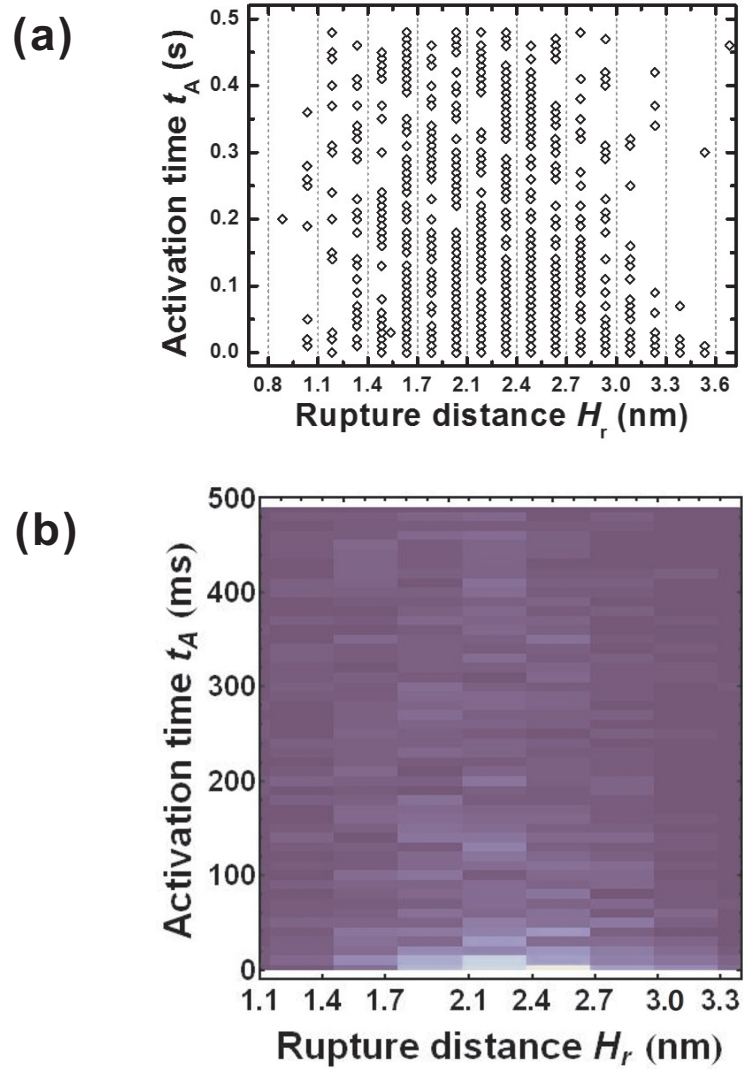


Figure 4.3: (a) Plot and (b) density plot of t_A versus H_r for rupture of the nanometer water bridge, which exhibits random distribution. This results shows that rupture process follows the Poisson statistics. The results are obtained on the ambient condition, RH = 35% and temperature 23.2 °C.

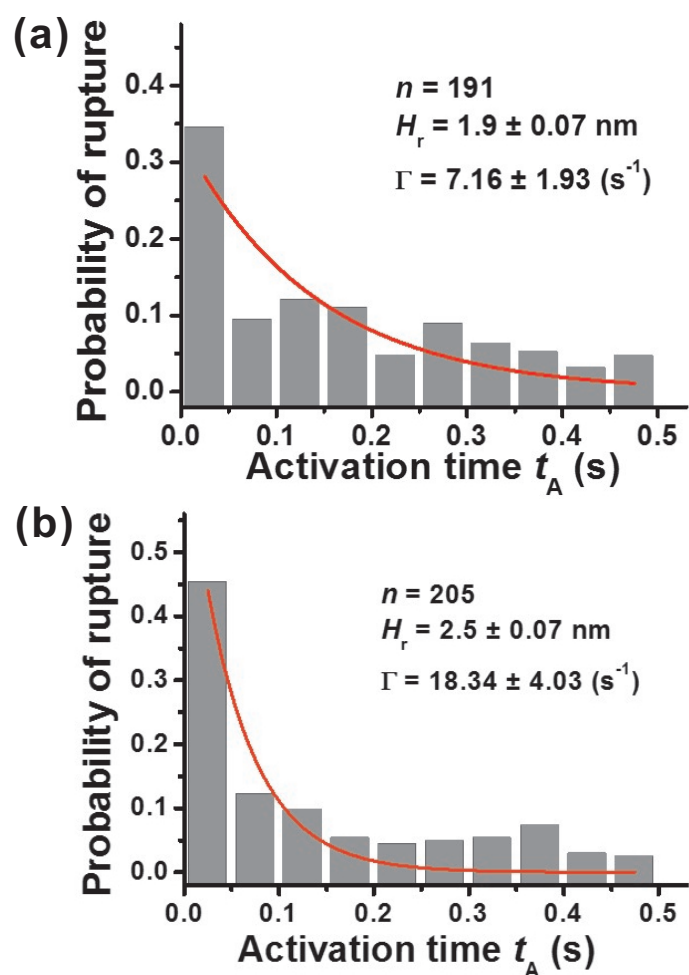


Figure 4.4: A histogram plotting the t_A at $H_r = 1.9$ and 2.5 ± 0.1 nm in Fig. 4.3 (a). This plot is obtained by the normalization by the total number of rupture events from $H_r = 1.76$ - 2.06 (a) and 2.37 - 2.67 nm (b). The t_A distribution shows the exponential decay behavior and fitted to an exponential decay (red line)

To study the distribution of t_A of each H_r , we classify the distribution t_A with respect to H_r by the unit interval of 0.3 nm. For each particular H_r , the t_A shows an exponential decay distribution, as it is exemplified in Figure 4.4 for $H_r = 1.9$ and 2.5 nm, where the each total number of occurrences is 191 and 205. This indicates that the rupture of the water nanobridge is governed by the rate, which is determined as the number of occurrences for the water nanobridge rupture per unit time.

Let $p(t)$ be the probability that rupture has not yet occurred until the time t , so that $p(t = 0) = 1$ where $t = 0$ corresponds to the instant time as the tip position is reaching at the H_r while tip is retracting from the sample. Thus the probability $p(t)$ is given by

$$p(t + dt) - p(t) = -\Gamma dt, \quad (4.1)$$

and thus

$$p(t) = \exp(-\Gamma t). \quad (4.2)$$

We found that the expression given in eq. 4.2 agrees with the distribution of t_A in Fig. 4.4. By fitting (red line in Fig. 4.4) the corresponding histograms of t_A to an exponential decay function (eq. 4.2), a rate is obtained for each H_r value studied. The rate is defined as the rate of the rupture process for the water nanobridge, and the rupture process follows the Poisson statistics [4].

According to previous methods, we obtained the dependence of the rupture rate Γ on rupture distance H_r for temperature $T = 23.2$ (as shown Fig.

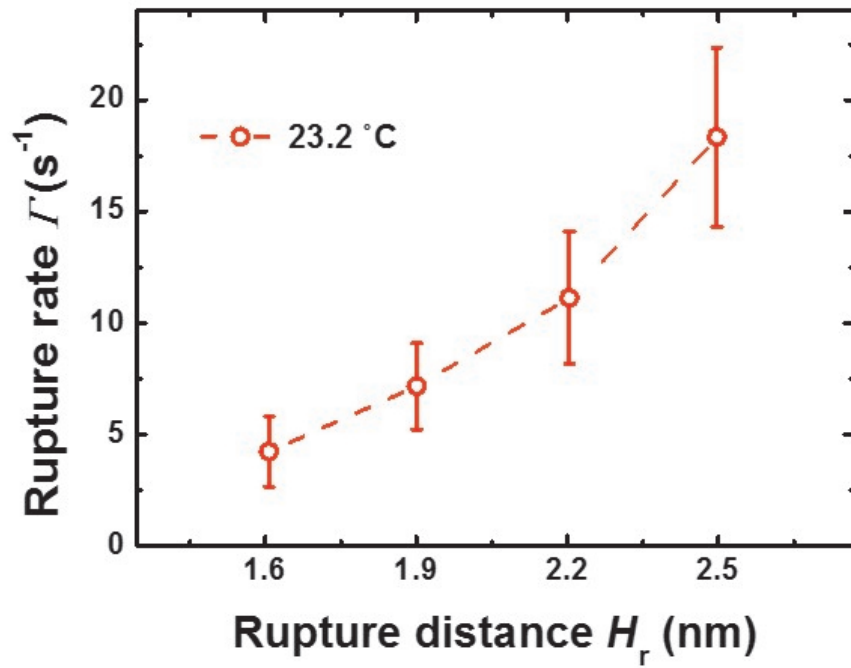


Figure 4.5: The rupture rate Γ as a function of H_r for temperature $T = 23.2$ (open circles) °C at RH 35%. Γ is obtained from the exponential fit for the distribution of activation time at a given H_r , as shown in Fig. 2(b). It shows that increasing the rupture distance H_r , increasing the rupture rate Γ .

4.5), where the each Γ is extracted from the slope of the exponential t by using eq. 4.2. The H_r range for temperature are the effective range for statistical analysis. We observe that increasing the tip-sample distance, increasing the Γ . This indicated that the more easier the water bridge breaks up as H_r increases. Thus, we infer that an increase of the tip-sample distance causes a decrease of the activation energy barrier that is originated from an increase of the rupture rate Γ .

We investigated the rupture rate Γ for different size of water nanobridge in Fig. 4.6. We obtained that the spatial distributions have the different peak position of rupture distance H_r in the same experimental conditions, temperature $T = 26.7$ °C, and RH $37 \pm 2\%$. In thermodynamic equilibrium, Riedo *et al.* [1] shows that the rupture distance of water nanobridge is related to the volume of water nanobridge. Because of different peak position in spatial distributions, it informed that the each spatial distributions is obtained to different size of water nanobridge. In Fig. 4.6 (b), we observed that the water nanobridge size increases as the rupture rate Γ increases. Because the size of water nanobridge increases as the capillary force strength increases, this indicated that the larger size of water nanobridge makes harder the water nanobridge rupture. In other words, an increase of the size of water nanobridge in a increase of the activation energy barrier, which leads to an decrease of the rupture rate Γ .

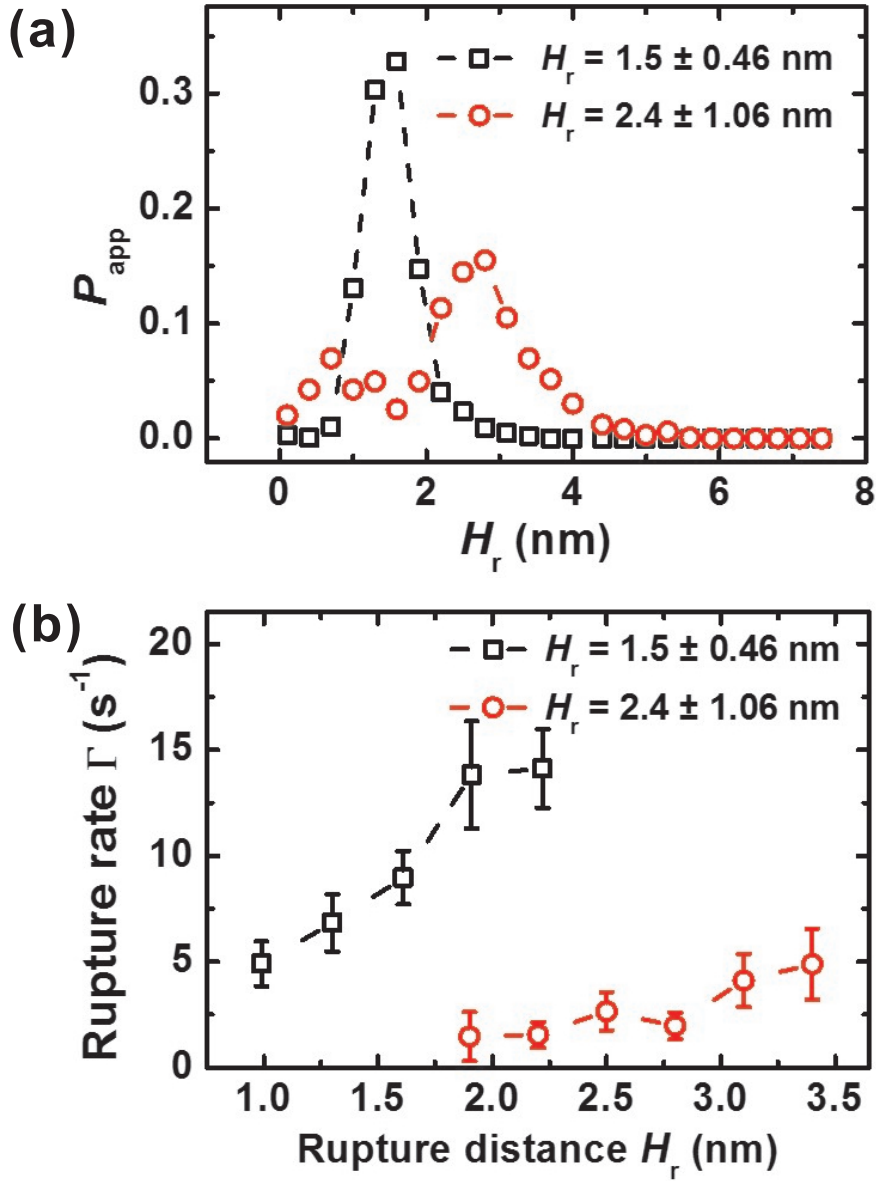


Figure 4.6: (a) The spatial distribution and (b) the rupture rate Γ as a function of H_r for different size of water nanobridge. The results are obtained on the ambient conditions, temperature $T = 26.7$ °C, and RH $37 \pm 2\%$. The each peak position of the spatial distribution in Fig. 4.5 (a) are $H_r = 1.5 \pm 0.46$ and 2.4 ± 1.06 nm. From the (a), we know that the spatial distributions have the different size of water nanobridge. The water nanobridge, which has the spatial distribution for large peak position, has the low rupture rate Γ on the rupture distance H_r [see of (b)].

4.3 Thermal Enhancement of Rupture Rate

To study a thermally activated process of the rupture process, we have repeated the approach-retraction cycles over one thousand times, similar to the previous experiments for various temperature $T = 20.7, 23.2$ and 26.7 °C at relative humidity 35-40 %.

We verified that it exhibits similar the each spatial distribution of H_r for the different temperature, as presented in Fig. 4.7 (a). We observed that the spatial distribution in each temperature have the peak position of the rupture distance H_r of ± 0.3 nm. Considering the peak position of each rupture distance H_r about 2 nm, we can be obtained the similar spatial distributions, see as Fig. 4.7 (b). Thus, the spatial distributions for different temperature is obtained at the same size of water nanobridge.

Fig 4.8 presents the rupture rate Γ on rupture distance H_r for various temperature, where the each Γ is extracted from the slope the exponential fit by using eq. 4.2. It shows that increasing the rupture distance H_r , increasing the rupture rate Γ . We observe that the temperature T increases, the rupture rate Γ increase.

Figure 4.9 presents the logarithmic plot of the rupture rate Γ of the $1/T$ at H_r , which is based on the Γ values for the temperatures T ($T = 20.7, 23.2$ and 26.7 °C) in Fig. 4.8. We obviously found that increasing the temperature T together with increasing the Γ . It indicates that the higher temperature leads to the enhanced rupture of nanometer water nanobridge. As the rupture of

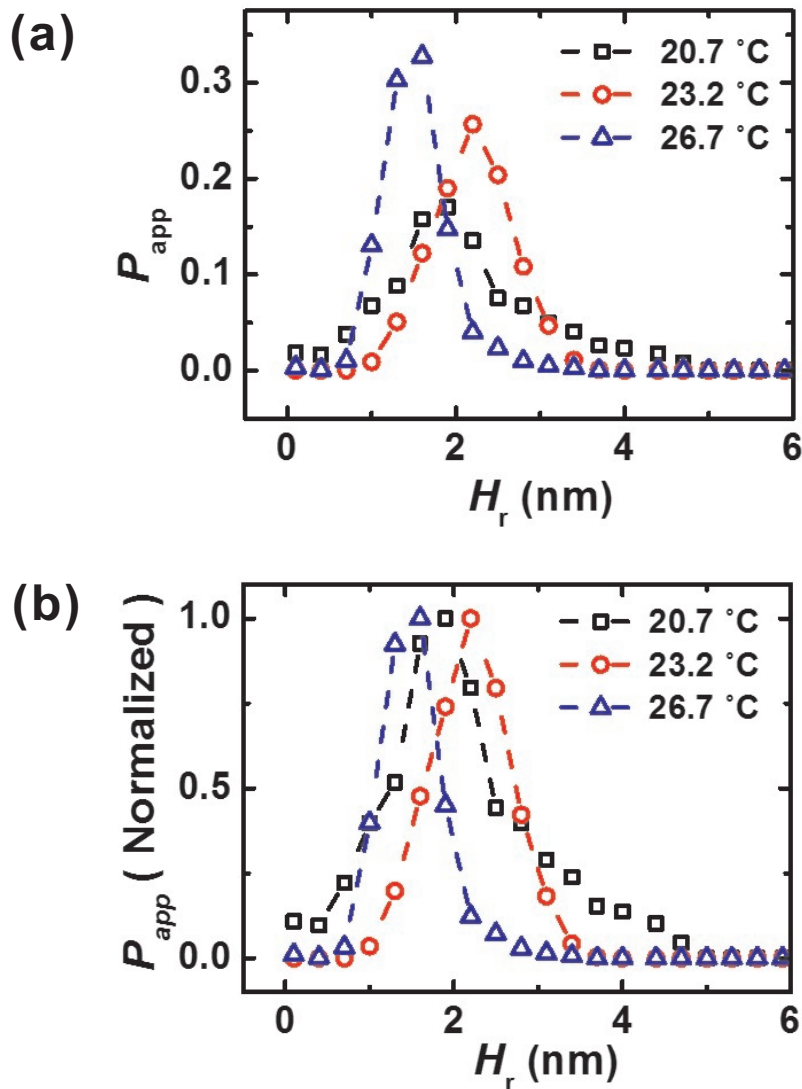


Figure 4.7: The spatial distribution as a function of the rupture distance H_r at the temperature T of 20.7 (open rectangles), 23.2 (open circles), and 26.7 °C (open triangles), while RH is maintained at $37 \pm 2\%$. We observed that the spatial distributions in each temperature have almost same peak position (± 0.3 nm) of the rupture distance H_r in (a). To see in detail in (a), we had normalized the P_{app} about maximum peak value of P_{app} (shown in (b)).

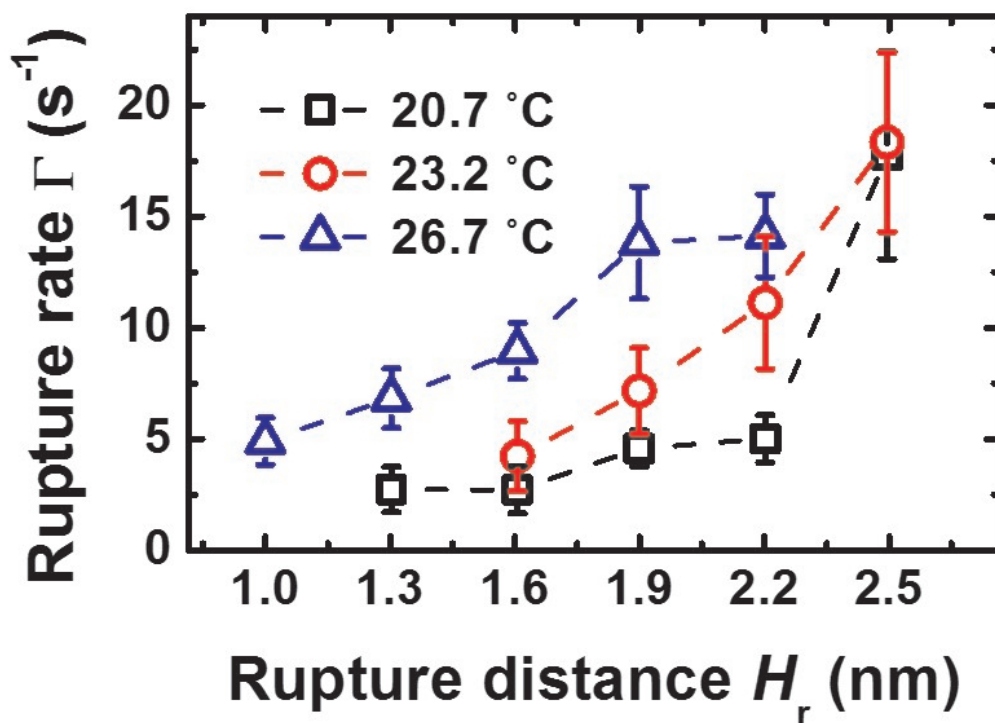


Figure 4.8: The rupture rate Γ as a function of the rupture distance H_r at the temperature T of 20.7 (open rectangles), 23.2 (open circles), and 26.7 °C (open triangles), while RH is maintained at $37 \pm 2\%$. Γ is obtained by the exponential fit for the distribution of activation time at a given H_r , as shown in Fig. 4.5. It is observed that Γ increases as the rupture distance H_r or the temperature T increases.

water nanobridge is the thermally activated process, the rupture rate Γ is associated energy barrier process that follows the Arrhenius law [5]. The Arrhenius equation, which relates the Γ given by

$$\Gamma = \Gamma_0 \exp\left(-\frac{\Delta\Omega}{k_B T}\right), \quad (4.3)$$

where Γ_0 is a prefactor, $\Delta\Omega$ is the activation energy, k_B is the Boltzmann constant, and T is the absolute temperature.

The energy barrier can be expressed as a function of the surface tension and contact angle [11]. $\Delta\Omega_{tot}$ is given by the sum of surface and volume contributions.

$$\Delta\Omega_{tot} = \gamma S(\cos\theta_1, \cos\theta_2) + aT, \quad (4.4)$$

where γ is the surface tension of interface, S is the surface area of the interface, T is temperature, a is the empirical constant, and $\theta_{1,2}$ is the tip-sample contact angle. However, the surface tension γ decreases with temperature increase, and its temperature variation can be described by the following simple equation:

$$\gamma(T) = -bT + c \quad (4.5)$$

with b the empirical constant and c is the surface tension of water at 0 °C [12].

Hence, the $\delta\Omega_{tot}$ can be presented by the following expression,

$$\begin{aligned}
\Delta\Omega_{tot} &= (-bT + c) \cdot S(\cos \theta_1, \cos \theta_2) + aT \\
&= T(a - bS(\cos \theta_1, \cos \theta_2)) + cS(\cos \theta_1, \cos \theta_2)
\end{aligned} \tag{4.6}$$

Applying the above equation, we find

$$\begin{aligned}
\Gamma &= \Gamma_0 \left(-\frac{\Delta\Omega_{tot}}{k_b T} \right) \\
&= \Gamma_0 \exp \left(-\frac{1}{k_b T} \cdot (T(a - bS(\cos \theta_1, \cos \theta_2)) + cS(\cos \theta_1, \cos \theta_2)) \right) \\
&= \Gamma_0 \exp \left(-\frac{1}{k_b} \cdot (a - bS(\cos \theta_1, \cos \theta_2)) - \frac{1}{k_b T} \cdot cS(\cos \theta_1, \cos \theta_2) \right) \\
&= \Gamma_0 \exp \left(-\frac{a - bS(\cos \theta_1, \cos \theta_2)}{k_b} \right) \cdot \exp \left(-\frac{cS(\cos \theta_1, \cos \theta_2)}{k_b T} \right) \\
&= \Gamma'_0 \exp \left(-\frac{\Delta\Omega'_{tot}(S(\cos \theta_1, \cos \theta_2))}{k_b T} \right)
\end{aligned} \tag{4.7}$$

where $\Gamma'_0(\Delta\Omega'_{tot})$ is the effective rupture rate (effective energy barrier).

Because the contact angle of the mica surface changes little below the boiling point, the temperature dependence of the rupture rate Γ is valid within the range of the temperature between the freezing and boiling temperature of water.

In Fig. 4.9 (a), we observe that the Γ values for each temperature correspond to the curve given by eq. 4.3. As fitting the experimental data to the eq. 4.3, we obtained the energy barrier $\Delta\Omega$ values (height of the energy barrier) for each H_r , which are estimated to be $(2.5 \pm 0.2) \times 10^{-19}$ J ($H_r = 1.6$ nm), $2.3 \pm 0.3) \times 10^{-19}$ J ($H_r = 1.9$ nm) and $(2.0 \pm 0.5) \times 10^{-19}$ J ($H_r = 2.2$ nm)

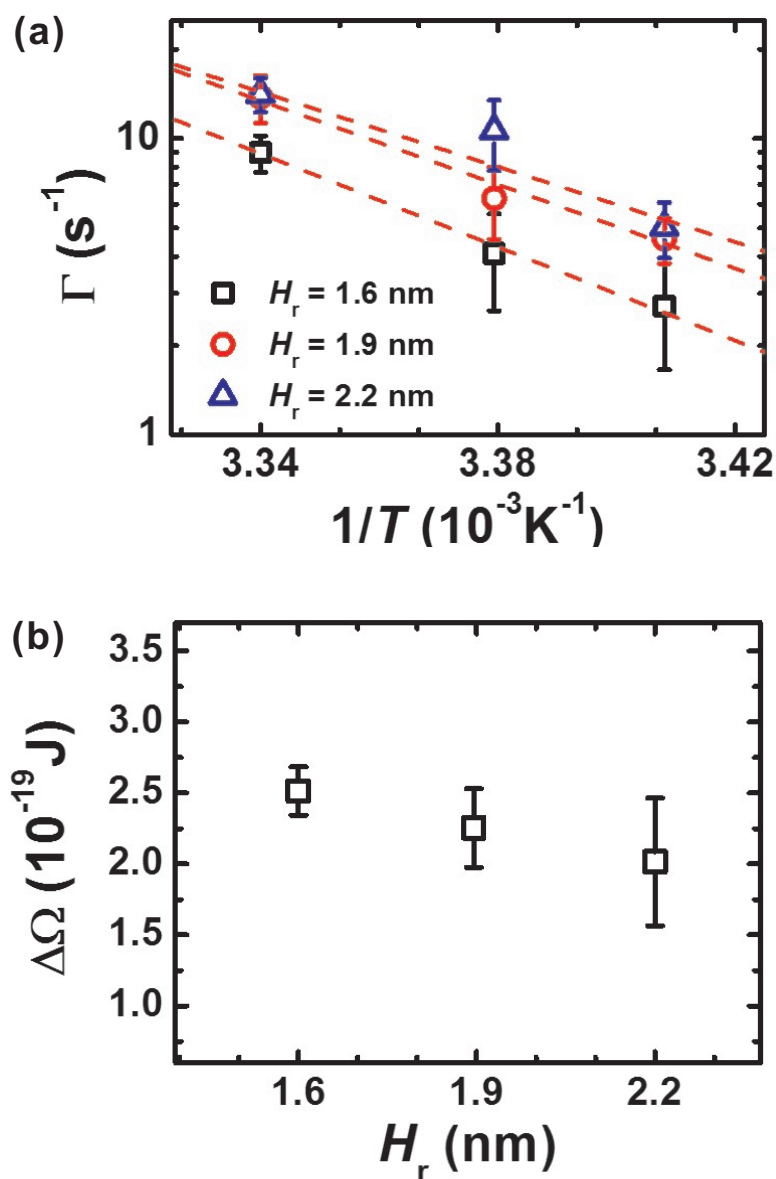


Figure 4.9: (a) Log-scale plot of the rupture rate Γ as a function of $1/T$ at $H_r = 1.6$ (open squares), 1.9 (open circles), and 2.2 nm (open triangles). The dashed lines represent the experimental fit of the Arrhenius equation, Eq. 4.3, obtained at T of 20.7 , 23.2 and 26.7 °C and at RH of $37 \pm 2\%$. (b) The energy barrier $\Delta\Omega$ is presented as a function of the rupture distance H_r , which is based on the fitting results of (a). The decrease of $\Delta\Omega$ with the increase of H_r suggests that the liquid-to-gas transition or the bridge rupture is more favorable at the larger distance.

as shown in Fig. 4.9 (b). From this results, we find that the longer the rupture distance H_r is the lower the height of the energy barrier $\Delta\Omega$. As we mentioned previously, further increasing the tip-sample distance, the more easily the water nanobridge ruptures.

As increasing the temperature and stretching water nanobridge, we could consider that there is changed the viscosity and the surface tension of the water nanobridge. The value for the viscosity of water differed by as much as 10 % in the temperature range from 20 to 26 °C [9]. From the experimental results, we observe the qualitative behavior that as the rupture distance H_r is longer, the energy barrier $\Delta\Omega$ becomes lower. Men *et al.* [6] have calculated the energy barrier associated with the formation and rupture of the water nanobridge as a function of tip-sample distance. Increase of the tip-sample distance makes the bridge rupture more favorable because the value of energy barrier for the bridge formation exceeds that of the bridge rupture. Our results are consistent with the theoretical result that further increase of the tip-sample distance lowers the energy barrier for the bridge rupture.

However, the thermally activated process for water nanobridge in rupture is not related with the surface tension rather than the viscosity. Also, we do not consider the viscosity of water nanobridge by the lateral force because of small oscillation of QTF (about 0.44 nm).

We shall consider a simplified model (see as Fig. 4.10). The homogeneous water nanobridge is assumed to have a constant curvature radius. For a given tip radius R_T and a tip-sample distance D , the pendular ring geometry of the

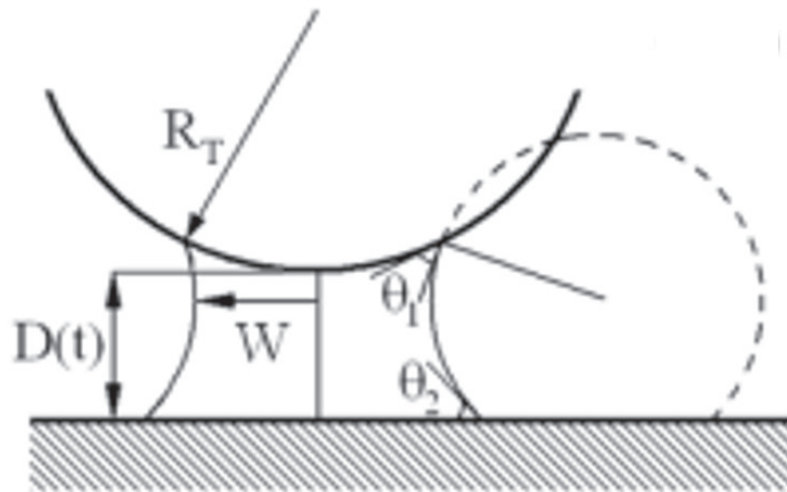


Figure 4.10: Sketch of the water nanobridge formed between a tip and flat sample. θ_1 and θ_2 are the tip surface and sample surface contact angles. The nanobridge neck diameter is W .

nanobridge [see Fig. 4.10] is characterized by the tip and sample contact angles θ_1 and θ_2 , respectively, and the nanobridge width W . The "excess" grand potential $\Delta\Omega_{tot}$ to rupture the water nanobridge is given by the sum of surface and volume contributions [5, 11]. The surface energy term is given by

$$\begin{aligned}\Delta\Omega_S &= S_{LV}\gamma_{LV} + S_{LS}(\gamma_{LS} - \gamma_{VS}) + S_{LT}(\gamma_{LT} - \gamma_{VT}) \\ &= \gamma[S_{LV} - S_{LS}\cos(\theta_2) - S_{LT}\cos(\theta_1)],\end{aligned}\quad (4.8)$$

where the S' s are the surface areas (the γ' s are the surface energies) of the liquid-vapor (LV), liquid-sample (LS), liquid-tip (LT), vapor-sample (VS), and vapor-tip (VT) interphases ($\gamma \equiv \gamma_{LV}$). At a given temperature T , the volume contribution :

$$\Delta\Omega_V = \gamma V \left(\frac{RT}{\gamma\theta_m} \ln(1/H) \right) \equiv \gamma V \frac{1}{r_k}, \quad (4.9)$$

where θ_m is the molar volume, R is the ideal gas constant, H is the relative humidity, and r_k is the Kelvin radius. Thus, the grand potential (energy barrier) to rupture the water nanobridge is dependent on the surface energy. However, the values for the surface tension of water in the range temperatures 20 - 26 °C differed at 1 % [10]. Thus, these results show that the thermally activated process for rupture in water nanobridge does not affect the viscosity and surface tension with temperature change.

It is interesting to notice that our measured $\Delta\Omega$ are about 20%-80% lower than the Men. *et al.* [6] reported value by the lattice density functional

theory. They study theoretically the hysteresis behavior of water nanobridge of H_r 10 nm for above RH = 80%, used to gold tip and sample which much more hydrophobic than mica [7, 8]. Because the capillary force have a stronger influence in high RH, the water nanobridge have the bigger size and the longer rupture distance. In other words, we expect that the longer rupture distance of water nanobridge in high RH, the higher energy barrier of $\Delta\Omega$. Nevertheless, Men *et al.* [6] and our observations show that increasing the rupture distance, decreasing the energy barrier height. So, this results can support the theoretical analysis about the rupture process in nanoscale.

Kwak *et al.* [13, 14] has predicted the gaseous bubble formation and the tensile strength of single liquids, such as water, CH_4 , and O_2 . His work can calculate the nucleation rate of the single liquids under negative pressure, which is associated with the energy barrier of the formation of the water nanobridge. From the water density on the temperature, they can obtain the effective molecular volume V_m ,

$$\frac{\pi}{6}(d_m)^3N = V_mN = 0.7405 \quad (4.10)$$

where 0.7405 is the packing fraction of a FCC lattice structure. Generally, the tensile strength at a given temperature is

$$\tau = P_\infty - P_v \quad (4.11)$$

where P_∞ is the ambient pressure, P_v is the vapor pressure.

But, in low temperature of room temperature, P_v is very small value in compared with P_∞ . Therefore, $\tau \sim P_\infty$ (in low temperature). The ambient pressure P_∞ is negative pressure, which taken of the water nanobridge. This negative pressure worked for the rupture of the water nanobridge.

The free energy of a molecular system is

$$F_N = P_\infty n V_m + \frac{1}{2} z \epsilon_m n^{2/3} \quad (4.12)$$

The stability condition for a water nanobridge requires that F_n is minimum with respect to n . The above equation shows that the minimum free energy occurs at $n = n_c$ when

$$-P_\infty n_c^{1/3} = \frac{2}{3} \left(\frac{\frac{1}{2} z \epsilon_m}{V_m} \right) = \frac{2}{3} \left(\frac{P}{V_m} \right) \quad (4.13)$$

If the intermolecular interaction force of the water nanobridge is the van der Waals force, the energy required to separate a pair of molecules ϵ_m is

$$\epsilon_m = 4\epsilon_0 \left[1 - \left(\frac{\rho_c}{\rho_m} \right)^2 \right] \left[\left(\frac{d_w}{d_m} \right)^6 - \left(\frac{d_w}{d_m} \right)^{12} \right] \quad (4.14)$$

where ρ_c is the density at the critical point and d_w is the van der Waals diameter of a molecule.

By eq. 4.10, 4.13 and 4.14, we can obtain the n_c . By inserting equations 4.13 and 4.14 into equation 4.12, the energy for the critical cluster F_{nc} is

$$\frac{F_{nc}}{kT} = \frac{z}{6} \left(\frac{\epsilon_m}{kT} \right) n_c^k \quad (4.15)$$

Table 4.1: The energy barrier height (F_{nc}) for the rupture of water nanobridge at different temperature (K), where ρ_m , P , n_c and F_{nc}/kT are the density of water, the pressure for water nanobridge at a given temperature, the number of the critical cluster and the free energy of the critical point divided kT.

Temperature(K)	$\rho_m(g/cm^3)$	P (mbar)	n_c	F_{nc}/kT	$F_{nc} (\times 10^{-19} J)$
20.7	0.9825	221.98	0.914×10^3	57.079	2.316
23.2	0.9820	220.37	0.930×10^3	57.259	2.358
26.7	0.9811	217.76	0.957×10^3	57.539	2.382

Hence, we can obtain the rupture rate dependence of the negative pressure for water nanobridge, which are given in Table 4.1.

However, this results are some different from our experimental results. Kwak's work is the energy barrier dependence of the negative pressure for water nanobridge, which its dependence of the negative pressure and temperature. But, our result is the energy barrier dependence of the tip-sample distance for the water nanobridge. Also, our result is obtained under constant pressure, because the driving oscillation amplitude of QTF is maintained by constant value. Thus, the difference in the results is originated from the viewpoint, such as whether or not it is changed negative pressure for water nanobridge. It is of great significance for the obtained energy barrier, which can be used the molecular cluster model for bubble formation.

4.4 Conclusion

In this chapter, our experimental results demonstrate an accessible approach to study the rupture process at nanoscopic liquid. We have directly measured the activation time of the rupture of the nanometer water nanobridge by using non-contact AFM. We observed that the distribution activation time is spread out over a wide range of rupture distance, and the each rupture events of nanometer water nanobridge is independent event. Also, the distribution of t_A for the H_r has the exponential decay behavior by statistical analysis. This show that the rupture is associated an activation process, the rupture process follows the Poisson statistics. Though the rupture rate Γ dependent for various temperature, we have confirmed that the Γ for $1/T$ agrees with the Arrhenius equation, and Γ related the activated energy barrier to overcome at the rupture of the water nanobridge. In addition, we observed that the rupture rate Γ is dependent on the tip- sample distance and temperature. There results show that the rupture process of the water nanobridge can be explained by the thermally activated process. By means of understanding the rupture mechanism, we expect to be extended and applied to the study of other liquid system as well as the rupture process of the water bridge in nanoscale.

Bibliography

- [1] L. Sirghi, R. Szoszkiewicz, and E. Riedo, *Langmuir* **22**, 1093 (2006).
- [2] J. Kim, D. Won, B. Sung and W. Jhe, *J. Phys. Chem. Lett.* **5**, 737 (2014).
- [3] B. Sung, J. Kim, C. Stambaugh, S-J. Chang and W. Jhe, *Appl. Phys. Lett.* **103**, 213107 (2013).
- [4] C. Stambaugh, and H. B. Chan, *Phys. Rev. B* **73**, 172302 (2006).
- [5] F. Restagno, L. Bocquet, and T. Biben, *Phys. Rev. Lett.* **84**, 2433 (2000).
- [6] Y. Men, X. Zhang, and W. Wang, *J. Chem. Phys.* **131**, 184702 (2009).
- [7] M. E. Abdelsalam, P. N. Bartlett, T. Kelf, and J. Baumberg, *Langmuir* **21**, 1753 (2005).
- [8] L. Xu, A. Lio, J. Hu, D. F. Ogletree, and M. Salmeron, *J. Phys. Chem. B* **102**, 540 (1998).
- [9] L. Korson, W. Drost-Hansen, and F. J. Millero, *J. Phys. Chem.* **73**, 34 (1969)

- [10] N. B. Vargaftik, B. N. Volkov, and L. D. Voljak, *J. Phys. Chem. Ref. Data* **12**, 817 (1983)
- [11] E. Sahagún, P. García-Mochales, G. M. Sacha, and J. J. Sáenz, *Phys. Rev. Lett.* **98**, 176106 (2007)
- [12] F. Cardarelli, *Materials handbook: a concise desktop reference, second edition*, (Springer, 2008)
- [13] H. Kwak, and R. L. Panton, *J. Phys. D* **18**, 647 (1985)
- [14] H. Kwak, J. Jung, and J. Hong, *J. Phys. Soc. Jpn.* **71**, 2186 (2002)

Chapter 5

Chapter 5

5.1 Summary and Perspective

In this thesis, the rupture process of water nanobridge was investigated by using time-resolved noncontact AFM.

In chapter 2, we presented that the quartz tuning-fork as force sensor is suitable to investigate the mechanical properties of water nanobridge. The cantilever-based AFM is occurred to jump-to-contact due to the capillary force in nanoscale. This problem is difficult to work the constant tip-sample distance. Also, in ambient condition, it is hardly to study the dynamic process of water nanobridge due to thermal drift. These problems is solved by using the quartz tuning-fork as force sensor, which has the high stiffness, sensitivity and is hardly affected by the temperature.

In chapter 3, we measured the AFM signal of water nanobridge by us-

ing QTF-AFM. QTF-AFM is advantaged in stable manipulation of water nanobridge, can be obtained the approach-retraction curves. From this process, we confirm the precise tip contact position of probe tip, and the elasticity, viscosity from the approach-retraction cycle.

In chapter 4, we introduced about the TRDFM and its applicability. Using TRDFM, we observed the real-time rupture process of water nanobridge. We measured the randomly the activation time for rupture, or the latency time required for the nanobridge breakup. By statistical analysis of the distribution of the activation time, we repeated the approach-retraction cycle over a few thousands. We show that the rupture rate Γ has the exponential decay curve for the rupture distance H_r . Increasing the H_r , increasing the rupture rate Γ , thus we confirm that increasing the tip-sample distance, easier the nanobridge breakup. These results informed that rupture is a thermally activated process and follows the Poisson statistics. From the temperature dependence of the rupture rate Γ , Γ follows the Arrhenius equation and should provide the energy barrier height.

Our time-resolved study offers a novel platform for a combined and unified understanding of the mechanics, dynamics and thermodynamic kinetics of the nanoscale interfacial liquid bridges in ambient condition.

Appendices

Appendix A

A.1 Phase behavior of rupture process for water nanobridge

Whether the water nanobridge is present or absent checked by the approach-retraction curve, amplitude signal of AFM. From this, we find the nucleation, rupture event and contact position. To define the nucleation and rupture position of water nanobridge, there is accurate the more phase signal of AFM. Because the phase signal change rate is larger than the amplitude signal change rate. From Fig. A.1, we observed same of the rupture position which is obtained both the amplitude signal data and phase signal data. To obtain accurate rupture position, we refer to the phase signal data of retraction curve.

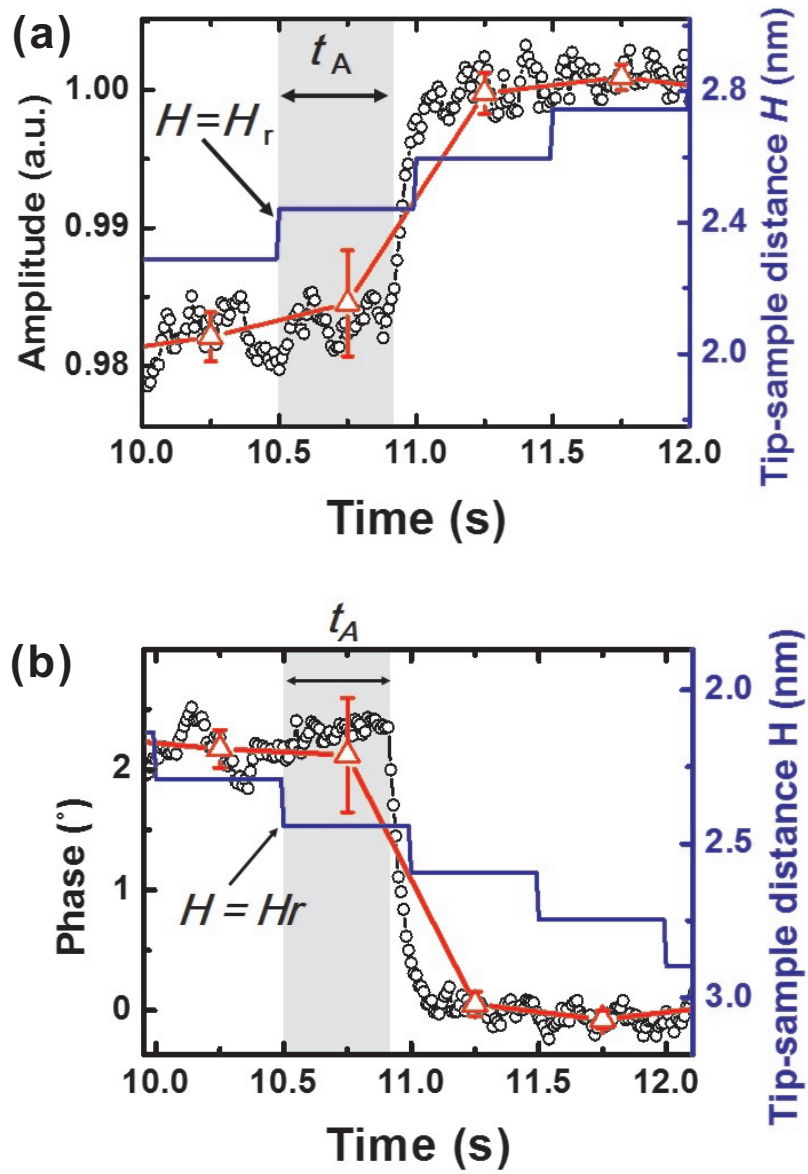


Figure A.1: The time-resolved amplitude (a) and phase (b) signal near the moment of rupture of the same water nanobridge. The real-time amplitude / phase (black open circles), its time-averaged amplitude / phase (red open triangles), and the tip-sample distance (blue line) are presented as a function of time. The activation time t_A is marked by the gray-filled area.

Appendix B

B.1 Actual and Apparent Probability

The rupture process for the water nanobridge can be considered as the Poisson process with the rupture rate $\Gamma^{(i)}$ where $i = 0$ corresponds to the position where the tip starts retracting the sample, so that the larger i corresponds to the larger tip-sample distance. Then the probability that there occurs exactly k occurrences of water nanobridge rupture in the given time interval t_s is equal to

$$f(k; \Gamma^{(i)} \cdot t_s) = \frac{(\Gamma^{(i)} \cdot t_s)^k \exp(-\Gamma^{(i)} \cdot t_s)}{k!}, \quad (\text{B.1})$$

where k is a non-negative integer. Such rupture process is irreversible because the liquid state is more stable than the vapor state, and thus the probability should be added for k ranging from unity to infinity. Then the probability $p_{act}^{(i)}$ is

$$p_{act}^{(i)} = P_{V \rightarrow L}(\Gamma^{(i)}, t_s) = 1 - \exp(-\Gamma^{(i)} \cdot t_s), \quad (\text{B.2})$$

which we call the actual probability at the i -th distance, in contrast to the apparent probability, as discussed below. The apparent probability $p_{app}^{(i)}$ at the i -th distance can be calculated from the experimental results, and it is defined by the number of occurrences of rupture divided by the total occurrences as a function of the distance. Then one can obtain the relationship between $p_{act}^{(i)}$ and $p_{app}^{(i)}$ as follows.

Let $X_i (i = 0, 1, 2, \dots, N)$ be the independent and actual events and Y_i be the exclusive and apparent events. Suppose that $p_{act}^{(i)} = P(X_i)$ and $p_{app}^{(i)} = P(Y_i)$, then $p_{act}^{(i)}$ is the conditional probability of $p_{app}^{(i)}$ given the complementary event of $(Y_0 \cup Y_1 \cup \dots \cup Y_{n-1})$, as written by

$$p_{act}^{(i)} = p_{app}^{(i)} / \left(1 - \sum_{j=0}^{i-1} p_{app}^{(j)} \right). \quad (\text{B.3})$$

Then, the rupture rate $\Gamma_s^{(i)}$ at the i -th distance is given by

$$\Gamma_s^{(i)} = -\frac{1}{t_s} \ln \left(1 - p_{act}^{(i)} \right), \quad (\text{B.4})$$

which can be calculated from the spatial distribution of the rupture occurrences.

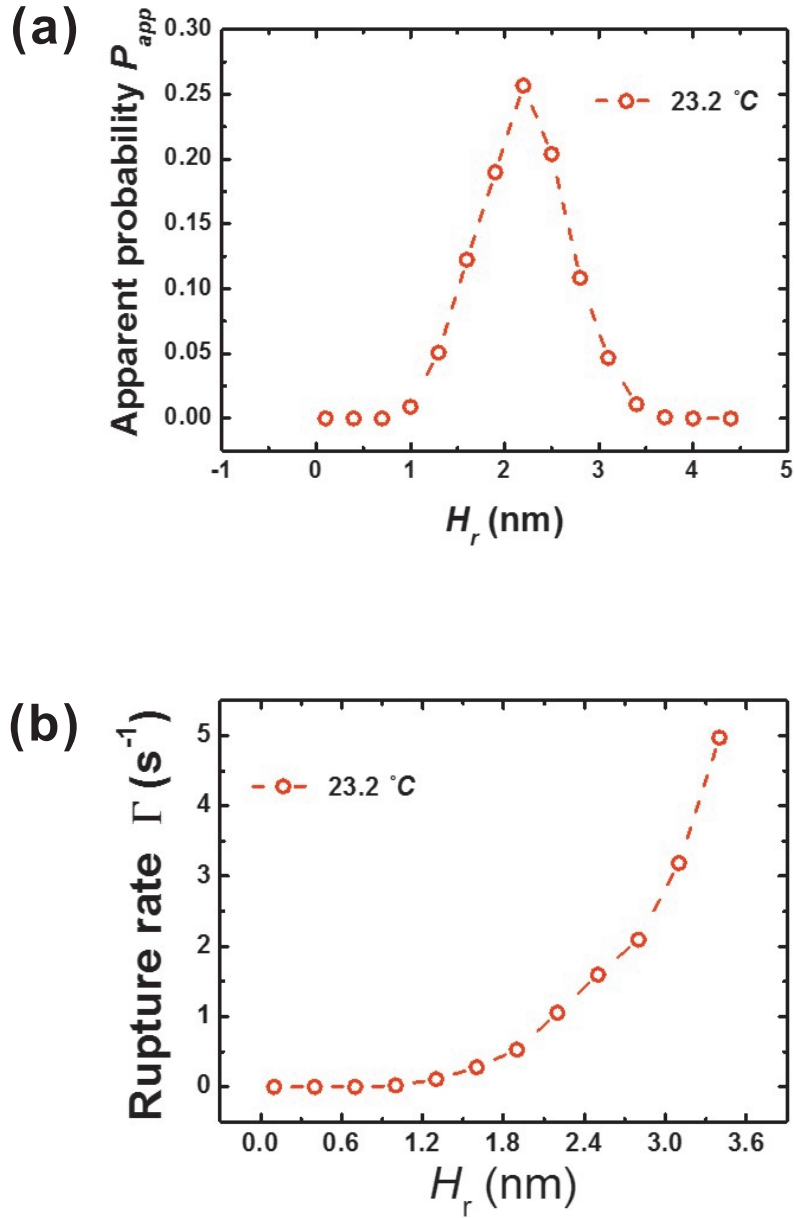


Figure B.1: (a) The apparent probability of the water nanobridge rupture as a function of the tip-sample distance. (b) The rupture rate Γ of the water nanobridge versus the tip-sample distance, as obtained from the spatial distribution of the apparent probability in (a).

Appendix C

C.1 Spectral fluctuations on excitonic transitions of InGaAs SQDs

1

C.1.1 Introduction

Recently, zero-dimensional quantum dots (QDs) have been investigated for potential applications in quantum information, quantum cryptography and optoelectronics, e.g., single photon source, light emitting devices [1]. Of particular interest is how one such confinement effect of a QD, the quantum confined Stark effect (QCSE), originates from spectral diffusion. Spectral diffusion is a well-known phenomenon [2, 3], which results from luminescence intensity quenching and random fluctuations of a single QD emission line [4]. The spectral diffusion

¹This chapter was modified and rewritten on the basis of the work which was submitted to Appl. Phys. Lett. **100**, 022105 (2012)

is manifested by carrier recombination processes or by an induced local electric field resulting from free carriers trapped in defects in the vicinity of the QDs [4, 5]. In fact, spectral diffusion of QDs has been related to the photoexcitation or neutralization of a QD which corresponds to changes in local electric fields [6].

The compounds, together with large self-compensation effects such as II-VI semiconductors, leads to have more charge defects than the III-V structures, making it more difficult to observe the spectral diffusion of III-V structures [7] using conventional optical spectroscopy [8]. But, Near-field scanning optical microscopy (NSOM) is a powerful tool for monitoring the effect of charge confinement in nanometer-sized QDs with less than subwavelength spatial resolution [9] and used to achieve this by measuring the optical properties of a single QD without sample processing, i.e., masking. Because the probe quality is close relative to the spatial resolution and sensitivity of NSOM measurement, probe fabrication is the heart of the NSOM [10].

In this chapter, we report on the spectral diffusion of single InGaAs QDs which does not easy observed using commercial NSOM probe but using improving NSOM probe, i.e., a double-tapered probe, in response to various excitation powers and applied electric fields. In particular, we show that the synchronous jitter, identified as synchronized fluctuations of the positions in time evolution of the emission lines, comes from single InGaAs QDs. These experimental studies of spectral diffusion in InGaAs QDs can provide information on the geometrical extent and internal structure of QDs.

C.1.2 Optical Fiber Probes for Low-Temperature Near-field Spectroscopy

To use the near-field probe, the outside surface of the probe is coated with metal, such as aluminum or gold, to prevent the illumination of excitatory light or the background signal through the side of the near-field probe. Because the metal coating probe has a complex loss mechanism, such as the cutoff diameter and absorption by the metal coating part, a critical problem has by its low throughput. The low throughput is originated from the existence of guiding loss in the metal coating tapered part. To decrease the guiding loss part, we produced the shorten length of the double tapered near-field probe. From this process, we expect the high throughput near-field probe.

Double tapered probe can be controlled by selective chemical etching method.

To investigate optical performance of near-field probes, we measured that the optical properties of gold coating thickness and distance between probe and light source as in Fig. C.1

Both double tapered probe and commercial aperture probe are similar to exponentially decay curve as distance. The single tapered probe represents far-field characteristics, but the double tapered probe shows near-field characteristics like as commercial aperture probe. In Fig. C.1, the transmittance of double tapered probe is more quickly decreasing than single tapered probe as increasing gold coating thickness. Therefore, double tapered probe can be applied as a near-field probe like as the commercial aperture probe.

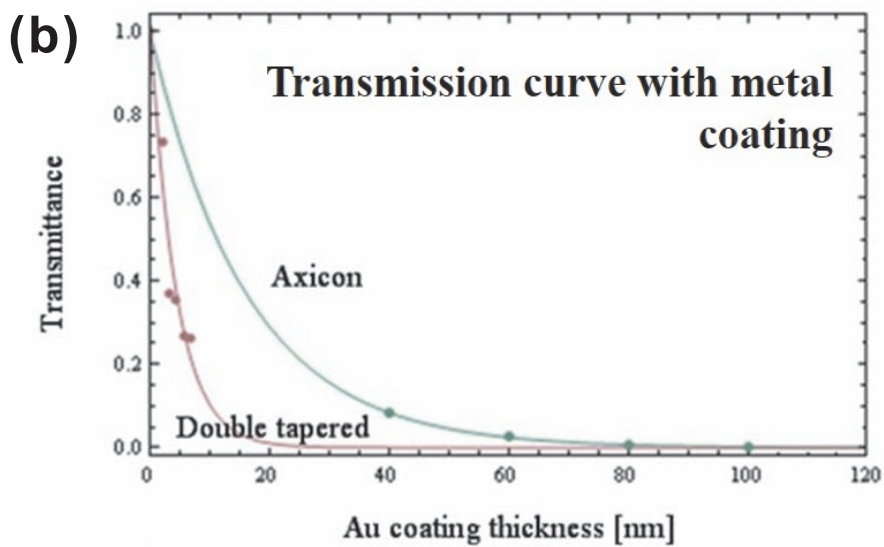
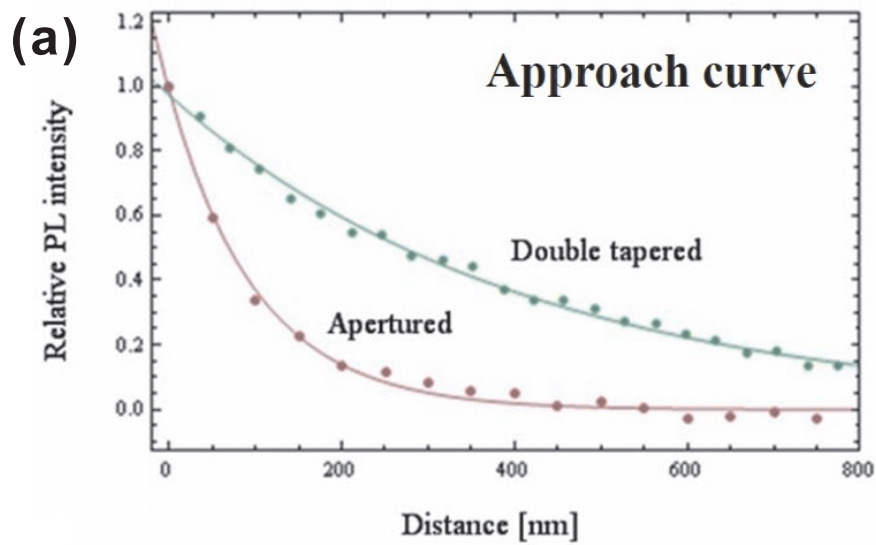


Figure C.1: (a) Optical curves of double-tapered and aperture NSOM probe. (b) Transmittance as function of Au coating thickness of double tapered and Axicon NSOM probe.

C.1.3 Spectral Random Fluctuation of InGaAs SQDs

A critical component of high-resolution NSOM is a well-defined probe shape which shortens the protrusion region, leading to less optical loss [10]. Our probe was fabricated using a two-step etching procedure in a hydrofluoric acid solution; the probe's tip diameter was about 10 nm and its apex angle was 90 degrees. In single molecule NSOM spectroscopy, the origin of spectral diffusion is charge trapped at the defects of the QDs and the light-confined metal tip [12]. However, here a bare double-tapered NSOM probe without metal-coating was used thus removing the charging effect at the metal-tip and allowing for direct observation of just the spectral diffusion at the InGaAs QD.

The self-assembled InGaAs QDs were grown on a GaAs buffer layer (100nm) of a n-doped GaAs substrate by molecular-beam epitaxy. Each QD had an average lateral dimension of 22 nm, a height of 7 nm, and a density of $8 \times 10^9 \text{cm}^{-2}$. The QDs were capped by a 30 nm thick layer of GaAs and a deposited Au/Ti electrode (10 nm). For optical excitation a Ti:sapphire laser, operating at 1.55 eV, coupled to a single-mode optical fiber and guided to a bare double-tapered NSOM probe, was used. All data presented in this paper were obtained from the photoluminescence (PL) signal at 77 K, with the NSOM operating in the illumination-collection mode [10,11]. The PL signal was dispersed by a 30 cm monochromator with a spectral resolution of 0.3 meV and detected using a liquid-nitrogen-cooled charge coupled device.

To study the relationship between spectral diffusion and defects of QDs,

we analyzed the PL spectra which is seen in the spectral diffusion. In Fig. C.2(a), the time evolution of the PL spectra is plotted and we label the specific peaks. Focusing our attention at energies between 1.29 eV and 1.31 eV, we can identify several emission lines displaying synchronous behavior (lines 3, 4 and 5). Each emission line shows a jitter amplitude of as little as 1meV [see Figure C.2(a)]. While the synchronous behavior is clearly seen in PL peaks 3, 4 and 5, PL peaks 1 and 2 do not demonstrate the behavior, see Figure C.2(b). In this case, PL peaks 1 and 2 do not seem to generate the spectral diffusion, though it is possible we are unable to observe it because of the spatial resolution of our NSOM is too high. The origin of the spectral diffusion can be seen by analyzing the NSOM images obtained at each peak. As each printed cross appears at the same position of the NSOM images [see Figure C.2(d)3-5], we clearly show that the emission peaks are obtained for a QD at the same position. In contrast, the other two peaks (peak 1, 2) emit from different QDs located within the range of spatial resolution. If the synchronous jitter appears in the vicinity of either the peaks marked by arrows 1 or 2, we can infer that the emission group for that peak originated from a single QD.

Also, we can consider that the origin of spectral diffusion is limited to only the QD structure, especially, defects of the QDs. The synchronous jitter of spectral diffusion is related to the QCSE of the QDs in a randomly local electric field. These fields result from the randomly captured or released charged carriers at defects in the vicinity of the QDs. The randomly fluctuating electric fields come from the randomly carrier density in the QDs, so it leads to individual

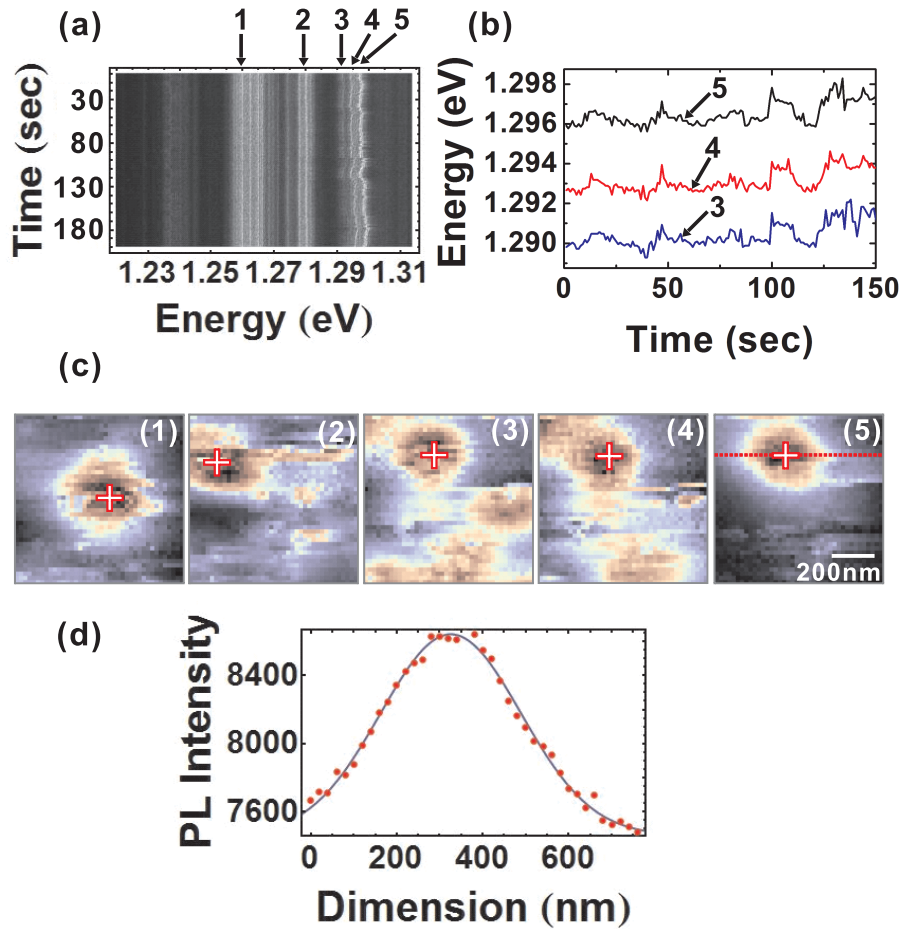


Figure C.2: (a) Time evolution of PL spectra: each time slice was averaged for 1 second. (b) Energy shifts of the peak 3, 4, and 5 for 150 seconds at an excitation power of 400 nW. The three peak traces exhibit synchronized energy fluctuations. Here the synchronous group lines are denoted as 3, 4, and 5, whereas the asynchronous peaks are denoted as 1, 2. (b) The line profile of the red dotted line (full width at half maximum (FWHM) 320nm) in (d)-(5). The line profile is fitted by a Gaussian curve to get the FWHM of the optical image, which is used to estimate the spatial resolution of the NSOM [15]. (c) Near-field images of each peak in the top of Fig. C.2(a). The image scan area is $800\text{ nm} \times 800\text{ nm}$ with a pixel size of 20 nm and the excitation power is 400nW. The crosses in Fig. C.2(c)(3)-(5) represent the center of the QD in the NSOM images.

Stark shifts. The jitter reflects the QDs geometry and carrier recombination and keeps going for several minutes [5]. This explanation is consistent with the observed excitation density dependence of the jitter amplitude; increasing the number of charged carriers together with increasing the excitation power density gives rise to stronger local fields and larger charge fluctuations at the defects of the QDs.

To understand the role of captured carriers in the spectral response we applied various excitation power densities to the sample, see Figure C.3(a)-(d). As the excitation power is increased the amplitude of the jitter response for the two peaks (1 and 2) is seen to increase. In Fig. C.3(e), the energy shift of peak 2 is plotted for all four excitation densities. Additionally plotting the standard deviation of the energy shift clearly illustrates the linear dependence, see Figure C.3(f). The excitation power dependence may be explained by the captured carrier in the vicinity of the QD. As the excitation power density increases, a larger number of carriers are generated in the vicinity of the QD. The captured carriers can give rise to the local static electric field, and interaction between the local electric field and the PL emission is observed for the spectral diffusion. Thus, the stronger spectral diffusion, the greater number of captured carriers.

Investigating the external field dependence of the QD can verify the quantum structure; such as the exciton characteristics. Here we examine the spectral diffusion in the presence of an external electric field. The bias voltage was applied between the back contact and the Ti/Au electrode on the InGaAs QDs sample like a gate, allowing for the control of the electron flow in the defect.

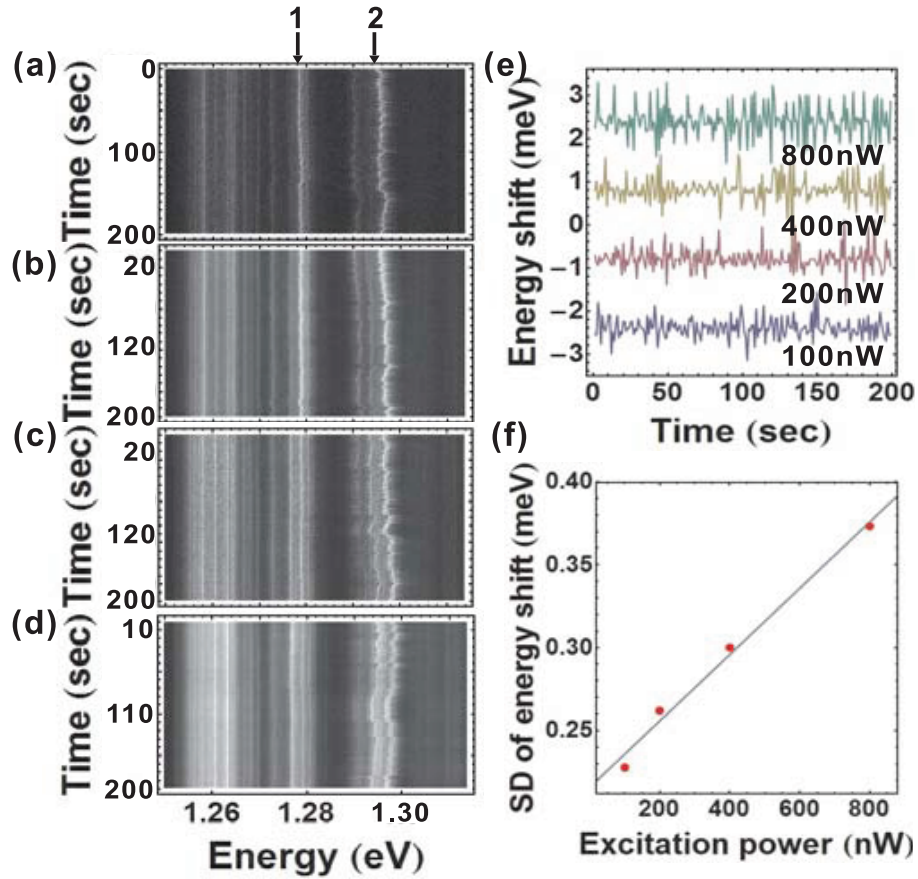


Figure C.3: [(a)-(d)] Time evolution of PL spectra showing the characteristic spectral fluctuation for different excitation powers: (a) 100nW, (b) 200nW, (c) 400nW and (d) 800nW. Two synchronous groups of emission lines are indicated by arrows 1 and 2. (e) The energy shifts in unit time (1 sec) of the brightest peak in group 2 for various excitation powers. (f) A linear fit of the standard deviation of unit time energy shifts as a function of excitation power for arrow 2 in graphs (a), (b), (c), and (d).

Figure C.4(a)-(d) show the time evolution of the spectral diffusion when the external electric field is varied from 0V to 3V. Here we can see that increasing the bias voltage leads to a weaker spectral diffusion pattern [16]. This means with increasing bias voltage, the defect electron levels are shifted below the Fermi energy E_F of the n-GaAs region, much like electric-field induced tilting of the potential barrier of QDs [5]. This results in increased electron occupation of the QDs via tunneling. Then it neutralizes the charged defects, which affects the field strength of the defects; a process known as neutralization [6].

As the applied electric field is increased, the carrier density at the defects decreases to a lower level, thus decreasing the fluctuation amplitude from the PL, i.e., spectral diffusion amplitude. We find that the spectral diffusion comes from the randomly changing carrier density at defects, which can affect the internal excitonic transitions in a QD. Synchronous jitter, which allows the identification of internal transition lines for a single QD, arises from the internal states of a single QD. Multi-exciton recombination in QDs, which has been observed in PL spectra of internal QD structures, provides further evidence that the spectral diffusion originates from local fields at defects. [17].

In conclusion, we have observed the spectral diffusion which is demonstrated by an induced local field at defects in the vicinity of single InGaAs QDs using improved double-tapered NSOM tip. Through the near-field PL image and spectra, we have confirmed that the synchronous jitter originated from single QD. By means of understanding the jitter mechanism, we know the carrier distribution, geometrical extent at defect [5] and internal structure in QDs [18].

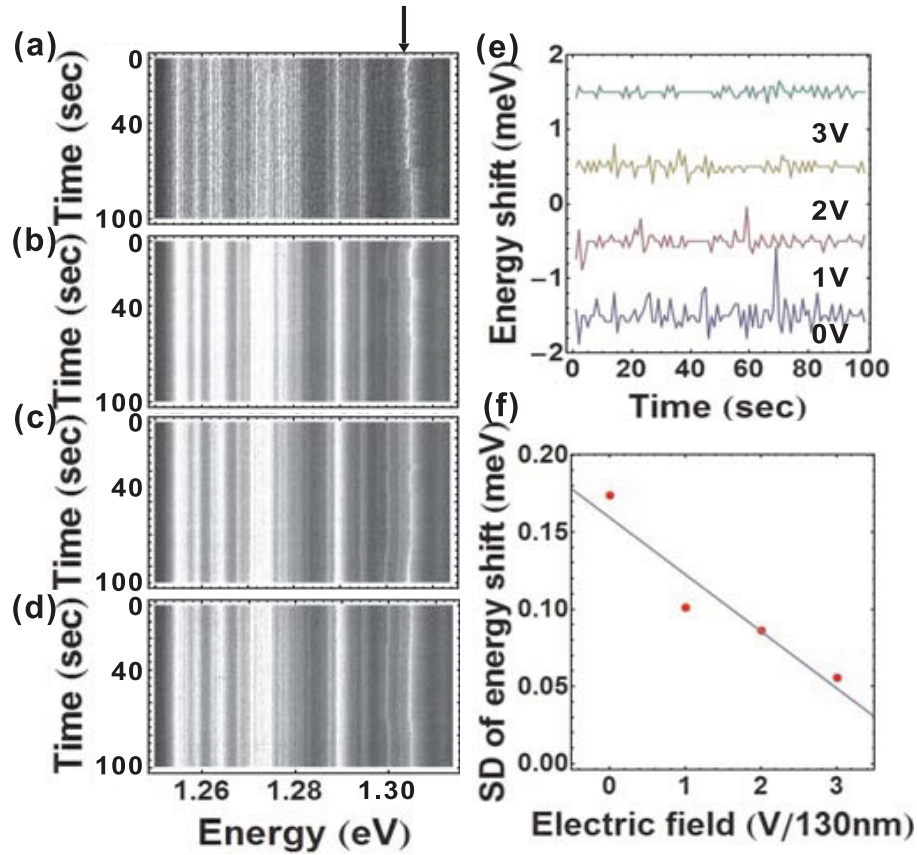


Figure C.4: [(a)-(d)] Time-integrated spectral diffusion for applied external electric fields at an excitation power of 400nW. (a) 0V, (b) 1V, (c) 2V and (d) 3V applied bias voltage. (e) The difference of energy shifts with 1 sec integration depending on various applied bias voltages. (f) A linear fit of the standard deviation of unit time energy shifts as a function of electric field at the specified arrow position. Of note here is how the increasing electric field decreases the jitter, while increasing excitation density increases it.

Therefore, this study provides detailed information about localized captured carriers and improvement of the FWHM.

Bibliography

- [1] V. Mantovani, S. Sanguinetti, M. Guzzi, E. Grilli, M. Gurioli, K. Watanabe, and K. Koguchi, *J. Appl. Phys.* **96**, 4416 (2004)
- [2] G.Sallen, A. Tribu, T. Aichele, R. André, L. Besombes, C. Bougerol, M. Richard, S. Tatarenko, K. Kheng, and J.-Ph. Poizat, *Phys. Rev. B* **84**, 041405(R) (2011)
- [3] G. Sallen, A. Tribu, T. Aichele, R. André, L. Besombes, C. Bougerol, M. Richard, S. Tatarenko, K. Kheng, and J.-Ph. Poizat, *Nature PHys.* **4**, 696 (2010)
- [4] J. H. Rice, J. W. Robinson, A. Jarjour, R. A. Taylor, R. A. Oliver, G. A. D. Briggs, M. J. Kappers, and C. J. Humphreys, *Appl. Phys. Lett.* **84**, 4110 (2004)
- [5] J. W. Robinson, J. H. Rice, K. H. Lee, J. H. Na, D. G. Hasko, R. A. Oliver, M. J. Kappers, C. J. Humphreys, G. A. D. Briggs, and R. A. Taylor, *Appl. Phys. Lett.* **86**, 213103 (2005)

- [6] N.Akopian, U. Perinetti, L. Wang, A. Rastelli, O. G. Schmidt, and V. Zwiller, *Appl. Phys. Lett.* **97**, 082103 (2010)
- [7] V. Türck, S. Rodt, O. Stier, R. Heitz, R. Engelhardt, U. W. Pohl, and D. Bimberg, *Phys. Rev. B* **61**, 9944 (2000)
- [8] S. A. Empedocles, and M. G. Bawendi, *J. Phys. Chem. B* **103**, 1826 (1999)
- [9] K. Matsuda, T. Saiki, S. Nomura, M. Mihara, Y. Aoyagi, S. Nair, and T. Takagahara, *Phys. Rev. Lett.* **91**, 177401 (2003)
- [10] T. Saiki, and K. Matsuda, *Appl. Phys. Lett.* **74**, 2773 (1999)
- [11] Y.-J. Yu, H. Noh, H.-R. Noh, T. Nakaoka, Y. Arakawa, and W. Jhe, *Phys. Rev. B* **82**, 085308 (2010)
- [12] X.S. Xie and R. C. Dunn, *Science* **265**, 361 (1994)
- [13] J.M. Imhof, E-S. Kwak and D.A.V. Bout, *Rev. Sci. Instrum.* **74**, 2424 (2003)
- [14] M. f. Garcia-Parajó, B.I. de Bakker, M. Koopman, A. Cambi, f. de Lange, C. G. Figdor, and N. F. van Hulst, *NanoBiotech.* **1**, 113 (2005)
- [15] K. Matsuda, T. Saiki, S. Nomura, M. Mihara, and Y. Aoyagi, *Appl. Phys. Lett.* **81**, 2291, (2002)

- [16] A. Berthelot, G. Cassabois, C. Voisin, C. Delalande, R. Ferreira, Ph. Rous-
signol, J. Skiba-Szymanska, R. Kolodka, A. I. Tartakovskii, M. Hopkinson,
and M. S. Skolnick, *New J. Phys.* **11**, 093032 (2009)

- [17] T. Bretagnon, P. Lefebvre, P. Valvin, R. Bardoux, T. Guillet, T. Taliercio,
and B. Gil, *Phys. Rev. B* **73**, 113304 (2006)

- [18] R. Bardoux, T. Guillet, P. Lefebvre, T. Taliercio, T. Bretagnon, S. Rousset,
B. Gil, and F. Semond, *Phys. Rev. B* **74**, 195319 (2006)

초 록

나노 크기 물기둥은 공기 중에서 두 물체가 매우 가까워졌을 때 모세관 응축현상 (capillary condensation)에 의해 자연스럽게 형성어지며, 매우 일반적인 자연 현상 중에 하나이다. 이러한 나노 크기 물기둥은 마찰, 흡착 그리고 윤향과 같은 역학적 과정에서 중요한 역할을 하고 있으며, 딥펜-나노식각 (dip-pen lithography), 원자힘 현미경 (atomic force microscopy)과 미세전자기계시스템 (micro-electro-mechanical system)을 포함한 나노기술에서 폭넓게 활용되어지고 있다. 최근 나노 크기 물기둥은 이온채널, 단백질접힘과 같은 생물학적 메커니즘 이해에 있어서 중요한 부분이라는 것은 잘 알려져 있다. 그러므로, 공기중에서 모세관 응축에 의한 물기둥의 형성부터 파열할때까지, 물기둥의 운동학 만큼 폭넓은 동역학적 이해가 중요하다.

지난 수십년간 모세관 응축에 의한 나노크기 물기둥의 형성에 관해 광범위한 연구가 이뤄지고 있었다. 이전에 많은 이론적 연구에 있어서, 켈빈-라플라스 방정식 (Kelvin-Laplace equation)은 고체 표면에 나노크기 접촉에 의해 형성된 물기둥의 크기와 모양을 결정하는데 사용되어 왔다.

특히, 열역학적 평형상태 (thermodynamic equilibrium)에서 형성된 물기둥은, 물기둥의 곡률반경이 켈빈 반지름과 같으며, 따라서, 물기둥은 켈빈 반지름의 두배만큼의 거리에서 끊어진다. 그러나, 나노범위안에서 모세관 응축에 의해 형성된 물기둥의 이러한 접근법을 활용하는 것은 여전히 많은 논쟁거리가 많은 것이 사실이다. 물기둥의 실험적 관찰 및 이론적 모델을 바탕으로 한 Riedo의 연구결과는 늘어진 물기둥의 부피는 파열거리에 비례한다는

사실을 보여주었다. 팁이 샘플로부터 멀어짐에 따라 물기둥의 곡률반경이 변화하기 때문에, 물기둥의 상태는 열역학적 평형상태에 있다고 할 수가 없다. 그러한 결과결부터, 늘어진 물기둥은 켈빈 반지름의 두배 이상의 거리에서 끊어진다.

열역학적 비평형상태에서 (thermodynamic nonequilibrium), 물기둥의 파열과정은 화학적 포텐셜 기울기 (chemical potential gradient) 에 관계하고 있으며, 이는 물질변화 및 비가역적 물기둥 파열을 촉발하는 결과를 가져온다. 그러므로, 켈빈 방정식은 열역학적 비평형상태에서는 적용하기가 어렵다. Yumie는 밀도함수이론 (density functional theory) 를 사용함으로써, 물기둥의 파열과정을 연구하였다. 그들의 작업은 물기둥의 형성 및 파열과정에 있어서 히스테리시스 형태의 원인을 설명하였다. 그리고, 물기둥의 파열과정은 에너지장벽을 극복함으로써 시작되며, 이것은 열적활성화과정 (thermal activation process) 이라고 한다.

그러나, 이론적 연구결과가 많음에도 불구하고, 열적활성에 관한 나노범위에서 파열과정 운동학에 관한 실험적 연구는 모세관형성과정에 비해 거의 없다.

본 논문에서는 공기중에서 수정진동차를 기반으로 한 원자힘현미경을 사용하여, 물기둥이 파열하는데 필요한 활성화시간 (activation time) 을 직접적으로 측정하였다. 우리는 파열거리에 대한 활성화시간이 랜덤분포를 가지는 것을 확인하였다. 또한, 이러한 활성화시간은 지수적 감소형태를 가지며, 이것은 파열과정이 푸아송통계를 따른다고 할 수 있으며, 열적활성화과정이라고 할 수 있다. 우리는 온도와 팁-샘플 거리에 대한 파열율의

의존성을 측정하였으며, 이로부터 활성화 에너지의 값을 계산하였다.

주요어 : 시간분해능 비접촉 원자힘 현미경, 수정진동자 원자힘 현미경,
나노물기둥, 파열, 열적활성화과정

학 번 : 2009-30096